

AD _____

Award Number: DAMD17-00-1-0291

TITLE: A Training Program in Breast Cancer Research Using NMR Techniques

PRINCIPAL INVESTIGATOR: Paul C. Wang, Ph.D.

CONTRACTING ORGANIZATION: Howard University
Washington, DC 20059

REPORT DATE: July 2005

TYPE OF REPORT: Annual

20060215 110

PREPARED FOR: U.S. Army Medical Research and Materiel Command
Fort Detrick, Maryland 21702-5012

DISTRIBUTION STATEMENT: Approved for Public Release;
Distribution Unlimited

The views, opinions and/or findings contained in this report are those of the author(s) and should not be construed as an official Department of the Army position, policy or decision unless so designated by other documentation.

REPORT DOCUMENTATION PAGEForm Approved
OMB No. 0704-0188

Public reporting burden for this collection of information is estimated to average 1 hour per response, including the time for reviewing instructions, searching existing data sources, gathering and maintaining the data needed, and completing and reviewing this collection of information. Send comments regarding this burden estimate or any other aspect of this collection of information, including suggestions for reducing this burden to Department of Defense, Washington Headquarters Services, Directorate for Information Operations and Reports (0704-0188), 1215 Jefferson Davis Highway, Suite 1204, Arlington, VA 22202-4302. Respondents should be aware that notwithstanding any other provision of law, no person shall be subject to any penalty for failing to comply with a collection of information if it does not display a currently valid OMB control number. PLEASE DO NOT RETURN YOUR FORM TO THE ABOVE ADDRESS.

1. REPORT DATE (DD-MM-YYYY)

01-07-2005

2. REPORT TYPE

Annual

3. DATES COVERED (From - To)

1 Jul 2004 - 30 Jun 2005

4. TITLE AND SUBTITLE

A Training Program in Breast Cancer Research Using NMR Techniques

5a. CONTRACT NUMBER**5b. GRANT NUMBER**

DAMD17-00-1-0291

5c. PROGRAM ELEMENT NUMBER**5d. PROJECT NUMBER****5e. TASK NUMBER****5f. WORK UNIT NUMBER****6. AUTHOR(S)**

Paul C. Wang, Ph.D.

E-mail: pwang@howard.edu

7. PERFORMING ORGANIZATION NAME(S) AND ADDRESS(ES)Howard University
Washington, DC 20059**8. PERFORMING ORGANIZATION REPORT NUMBER****9. SPONSORING / MONITORING AGENCY NAME(S) AND ADDRESS(ES)**U.S. Army Medical Research and Materiel Command
Fort Detrick, Maryland 21702-5012**10. SPONSOR/MONITOR'S ACRONYM(S)****11. SPONSOR/MONITOR'S REPORT NUMBER(S)****12. DISTRIBUTION / AVAILABILITY STATEMENT**

Approved for Public Release; Distribution Unlimited

13. SUPPLEMENTARY NOTES**14. ABSTRACT**

This is an extended 5th year of a training program. This program has supported four predoctoral students. One MD/PhD student suffered medical problem and his PhD thesis work has been delayed. The PI has filed a second extension of this grant in order to continue supporting the student and the research. All the trainees have continued to learn the theory and instrumentation of MRI. The trainees have attended the weekly seminars in the Cancer Center and also attended a special NMR seminar series in the Department of Radiology. They are also actively involved in one of the four ongoing research projects: (1) NMR studies of phosphorus metabolites of breast cancer cells using an improved cell perfusion system (2) Completion of a breast cancer image database for computed-aided-diagnosis (CAD) Research (3) A tumor-targeted nanodelivery system to improve early MRI detection of cancer (4) MRI and histological correlations of cortical brain volumes in APP/PS1 mice. One paper has been submitted to Molecular Imaging and it has been accepted for publication. Five abstracts have been presented in the national and international meetings. The PI has submitted two grant applications and he has received two new grants.

15. SUBJECT TERMS

Training, nuclear magnetic resonance, breast cancer

16. SECURITY CLASSIFICATION OF:**a. REPORT**
U**b. ABSTRACT**
U**c. THIS PAGE**
U**17. LIMITATION OF ABSTRACT**

UU

18. NUMBER OF PAGES

69

19a. NAME OF RESPONSIBLE PERSON**19b. TELEPHONE NUMBER (include area code)**

Table of Contents

Cover.....	1
SF 298.....	2
Table of Contents.....	3
Introduction.....	4
Body.....	4
Key Research Accomplishments.....	7
Reportable Outcomes.....	8
Conclusions.....	9
References.....	10
Appendices.....	12

I. INTRODUCTION

This is an extended 5th year of a training grant. This grant supports four predoctoral students (E. Chikezirim Agwu, Shani Ross, O'tega Ejofodomi and Armand Oei) for pursuing breast cancer research using NMR technique. There are three other postdoctoral fellows (Lisa Kinnard, Ercheng Li and Renshu Zhang), who were supported by this grant in the previous years, also participated in the ongoing research projects.

Dr. Agwu is a MD/PhD student in the Department of Molecular Biology and Biochemistry. Dr. Agwu has received a MD degree in year 2003 and is continuing his PhD program. Dr. Agwu has an inherited sickle cell disease. He was hospitalized several times during the year. The extension of this grant is to support Dr. Agwu to complete his PhD pursue and also allow other students to finish the research projects. During the year, Dr. Agwu has submitted a PhD thesis proposal.

Ms. Ross and Ms. Ejofodomi graduated from the Department of Electrical Engineering in 2004. They have gone to graduate schools for biomedical engineering studies. Although Ms. Ross' and Ms. Ejofodomi's research and training have been presented in the last year's annual report, the progress of their training is also included here in this report because their employment extended into September 2004. Mr. Oei was an intern working on a project to explore the application NMR molecular imaging techniques developed in this program in detection of amyloid plaques in the Alzheimer diseased mouse brain. Mr. Oei has been accepted to a professional optometry school. Dr. Lisa Kinnard graduated from the Department of Electrical Engineering in June 2003 and continued as a postdoctoral fellow at Howard University Cancer Center. Dr. Kinnard received a postdoctoral grant in 2004. Dr. Ercheng Li is a NMR/MRI specialist. Dr. Renshu Zhang is a radiologist. Both Dr. Li and Dr. Zhang are research associates.

All the trainees have attended the weekly seminars in the Cancer Center and a special NMR imaging seminar series in the Department of Radiology. Each trainee has actively participated in one of the four research projects. The details of the each project are listed in the section II of this report. Based on the experimental findings, one paper has been submitted and accepted for publication; five abstracts have been presented in national and international scientific meetings. The PI has submitted two grant applications and has rewarded two grants. A list of the publications and presentations are included in the reportable outcomes section.

II. BODY

In this year we concentrated our research efforts in four areas. Three projects are continuation from the previous research. The fourth one is to utilize the molecular imaging technique to exploit new application in imaging of amyloid plaques in Alzheimer disease. A abridge of each project is listed as following:

- (1) NMR Studies of Phosphorus Metabolites of Breast Cancer Cells Using an Improved Cell Perfusion System (Agwu, Li)

P^{31} NMR has been used to study the high energy phosphorus metabolites in tumors. It can be used to monitor the effectiveness of cancer treatment. Since the NMR signals of the phosphorus metabolites in cells are weak and the NMR study usually are long. During the long

data acquisition time, the cancer cells need to be maintained in a good living environment. In this project, we developed an improved NMR cell-perfusion system, which was used to study the phosphorus metabolites of breast cancer cells for an extended period. The improved perfusion system is driven by a peristaltic pump. The portion of the system before the pump is under negative pressure, and the portion after the pump is under positive pressure. This design helps the removal of air bubbles trapped in the perfusion medium and avoid the degradation of the quality of NMR spectrum. Using this perfusion system, NMR study of the breast cancer cells can be extended for more than a week not hours as it used to be. The ^{31}P NMR spectrum of the wild type MCF7 breast cancer cells shows three distinct phases, which reflect the proliferation of the cells. Study of oxygenation of the agarose-encased cells in this perfusion system suggests that the cells utilized aerobic respiration. The ability for this perfusion system to maintain cells viable for more than a week allowed us to determine the longitudinal relaxation times (T1 values) of the ^{31}P metabolites of MCF7/WT cells *in vitro*. A progressive saturation recovery NMR technique was used for T1 measurement. Accurate T1 values are crucial in designing P^{31} MRS studies. This study has demonstrated that the long time bubble-free NMR cell perfusion system could be a useful tool for *in vitro* breast cancer research.

(2) Completion of a Breast Cancer Image Database for Computed-Aided-Diagnosis (CAD) Research (Kinnard, Ross, Ejofodomi)

In the summer of 2004, we have completed digitization of 1000 mammograms from 220 African American breast cancer patients. This breast cancer mammographic image database will be available on the internet and it can be used for the CAD software research and development. The success of CAD is based on the accuracy and completeness of the mammographic image database, of which the CAD extracts the features of different types of pathology. The current available mammographic image databases are all obtained from the Caucasian population. There are very few African American cases. It is well known that African American women generally have denser breasts. The appearance of mammograms from African American breast cancer patients may not be the same as those images from Caucasian breast cancer patients. Howard University Cancer Center has a well maintained cancer registry. It has more than 200 new African American breast cancer cases each year. The completion and the availability of this African American breast cancer mammographic image database will improve the research and development endeavors in the CAD community.

(3) A Tumor-Targeted Nanodelivery System to Improve Early MRI Detection of Cancer (Li, Zhang, Song)

The development of improvements in Magnetic Resonance Imaging (MRI) that would enhance sensitivity, dealing to earlier detection of cancer and visualization of metastatic disease is an area of intense exploration. We have devised a tumor targeting, liposomal nanodelivery platform for use in gene medicine. This systemically administered nanocomplex has been shown to specifically and efficiently deliver both genes and oligonucleotides to primary and metastatic tumor cells, resulting in significant tumor growth inhibition and even tumor regression. In this research we examined the effect on MR imaging of incorporating conventional MRI contrast agent Magnevist into an anti-transferrin receptor single chain antibody (TfRscFv) liposomal complex. Both *in vitro* and in an *in vivo* orthotopic mouse model of cancer showed an increased

resolution and image intensity with the complexed Magnevist. Using advanced microscopy techniques (SEM and SPM) it has shown that the Magnevist is in fact encapsulated by the liposome in the complex and that the complex still retains its nano-dimensional size. These results demonstrate that the TfRscFv-Liposome-Magnevist nanocomplex has the potential to become a useful tool in early cancer detection.

(4) MRI and Histological Correlations Of Cortical Brain Volumes In APP/PS1 Mice
(Oei, Song)

Quantitative analyses indicate that brain atrophy on ante-mortem neuroimages and post-mortem tissue strongly correlates with the severity of cognitive impairment in Alzheimer's disease (AD). The absence of cortical atrophy in the age-matched, non-demented elderly suggests that volumetric studies of ante-mortem neuroimages may provide an early marker of AD in aging populations. In this study we used design-based stereology to quantify cortical volumes in double transgenic mice that deposit AD-type mutant β -amyloid proteins ($A\beta$) in cortical tissue. Spin-echo T1-weighted, high-resolution magnetic resonance imaging (MRI) was applied to the brains of male and female double transgenic mice aged 4-28 months of age that co-express AD-type mutations in amyloid precursor protein (APP) and presenilin-1 (PS-1), and, age-matched non-tg littermate controls (wild-type, WT). From a systematic-random series of coronal MRI images, total volumes of the hippocampal formation (V_{HF}) and whole brain (V_{brain}) were quantified by the Cavalieri-point counting method. The same sampling and estimation methods were used to quantify the same brain regions after perfusion and tissue processing. Strong correlations were found between V_{HF} and V_{brain} estimates from MRI images and histological sections. Agonal and tissue processing changes accounted for about 65 to 75% differences in cortical volumes between *in situ* and coverslipped sections. No differences were present in mean V_{HF} or mean V_{brain} for dtgAPP/PS1 compared to WT mice. These stereological studies of MRI neuroimages and postmortem tissue do not show cortical atrophy in association with widespread cortical deposition of AD-type amyloid plaques in aged dtg APP/PS1 mice, in contrast to the severe cortical atrophy in AD. Future studies with dtgAPP/PS1 mice will explore the possibility that high contrast ligands bound to mutant $A\beta$ proteins associated with amyloid plaques could facilitate early diagnosis of AD by ante-mortem neuroimaging.

The progress in training and research aligned with the Statement-of-Works is summarized as following:

Statement of Work: (year 5, an extended year)

Predoctoral Student:

• **Conclude the thesis project and write up thesis**

Mr. Armand Oei has finished his internship in the lab and was accepted to the New England School of Optometry. Dr. E. Chikezirim Agwu is a MD/PhD student. He received a MD degree in 2003. During the last two years, Dr. Agwu was continuing pursuing his doctoral degree in the Department of Molecular Biology and Biochemistry. Dr. Agwu's research has been delayed due to his health condition. The PI and his thesis committee members had a thorough discussion of Dr. Agwu's situation and decided to continue support

his pursue to complete his Ph.D. thesis. In year 2004, Dr. Agwu has submitted a Ph.D. thesis proposal. Dr. Agwu will continue his research in NMR study of phosphorus metabolites in breast cancer cells. The PI has submitted a second extension of this grant in order to continue to support Dr. Agwu and his research.

- **Thesis defense and writing of scientific papers for publication**

Dr. Agwu's has presented a paper in the 4th RCMI International Symposium on Health Disparities in December 2004. He plans to finish his thesis work this year.

Postdoctoral Student:

- **Select a new research project approved by the Executive Committee**

There are two research projects that have been developed this year:

- (1) A Tumor-Targeted Anti-transferrin Receptor scFv-Immunoliposome Nanodelivery System to Improve Early MRI Detection of Cancer (Dr. Li and Dr. Zhang)
- (2) MRI and Histological Correlations Of Cortical Brain Volumes In APP/PS1 Mice

- **Clinical preceptorship (half a day per week)**

This task was completed in year 2004 and it was reported in the last annual report.

- **Conduct the new research project**

- (1) Dr. Li and Dr. Zhang have constructed anti-transferrin receptor single chain variable fragment immunoliposome nanoparticles to carry MRI contrast agents specifically targeting cancer cells to improve the MRI image contrast. Based on these initial results, we have submitted a grant application to NIH/NCI this year.
- (2) We are continuing to develop a research program using MRI imaging technique to study the precursor protein of plaques in the double transgenic mouse brain to simulate brain imaging of the Alzheimer disease for early detection.

- **Present progress report to the Executive Committee once every six months**

The progress of the research was reported to the Executive Committee routinely.

- **Present research results to the Cancer Center faculty and National Meeting**

Five papers have been presented in the national and international meetings.

- **Writing Scientific papers**

The trainees and PI have published one paper. Another paper is in preparation.

III. KEY RESEARCH ACCOMPLISHMENTS

- An improved NMR cell-perfusion system was developed. It has been used to study the phosphorus metabolites of breast cancer cell for an extended period longer than one week. Using this perfusion system, the T1 relaxation times of phosphorus metabolites were accurately measured.
- The image digitization of more than 1000 mammograms from 220 African American breast cancer patients has completed. This huge image database is available to be used in the further development of Computer-Aided-Diagnosis (CAD) system.
- MRI contrast agent is incorporated into an anti-transferrin receptor single chain antibody (TfRsc) liposomal nanoparticle for MRI molecular imaging. This significantly improves the image contrast between tumor and surrounding tissues. This improves the specificity of MRI imaging of tumor.

- No differences were present in either the total brain volume or hippocampus volume between the double transgenic APP/PS1 mice, as a Alzheimer disease model, and the wild type mice.

IV. REPORTABLE OUTCOMES

Research

Manuscripts

1. Kinnard L, Lo S-C.B, Wang PC, Freedman MT, Chouikha M, Separation of Malignant and Benign Masses Using Image and Segmentation Features. Proc. of SPIE, 2003 (This was listed as 'in press' in the 2003 annual report and it was not included in the Reportable Outcome in the 2004 annual report. The reviewer for 2004 annual report suggested this to be included in this year's Reportable Outcome.)
2. Kinnard L, Lo SB, Makariou E, Osicka T, Wang P, Chouikha MF, Freedman MT. Steepest changes of a probability-based cost function for delineation of mammographic masses: A validation study. Med. Phys. 31(10):2796-2810, 2004. (This was presented in 2004 Annual Report as a paper accepted for publication).
3. Pirollo K, Dagata J, Wang PC, Freedman M, Vladar A, Fricke S, Ileva L, Zhou Q, Chang EH. A Tumor-Targeted Nanodelivery System to Improve Early MRI Detection of Cancer. (Accepted for publication in *Molecular Imaging*).
4. Manaye KF, Wang, P, O'Neil J, Oei A, Song HF, Tizabi Y, Ingram DK, Mouton PR. MRI and Histological Correlations Of Cortical Brain Volumes In APP/PS1 Mice. (in preparation)

Presentations

1. Wang PC, Li E, Zhang R, Song H, Pirollo K, Chang EH. MR Image Enhancement by Tumor Cell Targeted Immunoliposome Complex Delivered Contrast Agent. Society for Molecular Imaging 3rd Annual Meeting, September 9-12, 2004, St. Louis, MO. (This was included in the 2004 Annual Report).
2. Manaye KF, Wang PC, O'Neil J, Oei A, Song H, Tizabi Y, Ingram DK, Mouton PR. In vivo and In vitro Stereological Analysis of Hippocampal and Brain Volumes in Young and Old APP/PS1 Mice Using Magnetic Resonance Neuroimages. Society of Neuroscience 34th Annual Meeting, October 23-27, 2004, San Diego, CA. (This was included in the 2004 Annual Report).
3. Wang PC, Aszalos A, Li E, Zhang R, Song HF, Malveaux R. Increased Transport of Trifluoperazine Across the Blood-Brain-Barrier Due to Modulation of P-glycoprotein. 9th RCMI International Symposium on Health Disparities. December 8-11, 2004, Baltimore, MD.
4. Agwu CL, Zhou J, Li E, Sridhar R, Wang PC. NMR Studies of Phosphorus Metabolites of Breast Cancer Cells Using An Improved Cell Perfusion System Applications for the Improved NMR Perfusion System for Breast Cancer Cell Study. 9th RCMI International Symposium on Health Disparities. December 8-11, 2004, Baltimore, MD.
5. Manaye KF, Wang PC, O'Neil J, Oei A, Song HF, Tizabi Y, Ingram DK, Mouton PR. In-Vivo and In-vitro Stereological Analysis of Hippocampal and Brain Volumes in Young and

Old APP/PS1 Mice Using Magnetic Resonance Neuroimages. 9th RCMI International Symposium on Health Disparities. December 8-11, 2004, Baltimore, MD.

Career Development

Grants and other Funding

Applied for:

- Comparison of MR and Optical Imaging for the Metastatic Tumor Detection Using a Nano Delivery Complex. This was submitted on 3/28/05 as a pilot project in an application to the 'NIH/NCI Centers of Cancer Nanotechnology Excellence' Center Program. Dr. Esther Chang is the PI.
- Tumor-targeted MR Contrast Enhancement Using Molecular Imaging Techniques. This was submitted as a competitive renew for the National Cancer Institute's Minority Institution/ Cancer Center Partnership (MI/CCP) Program in year 2005-2006.

Received:

- A Partnership Training Program in Breast Cancer Research Using Molecular Imaging Techniques. This is a four year training grant partnership with the Johns Hopkins University, In vivo Cellulose and Molecular Imaging Center. The proposal is funded by the U.S. Army Medical Research and Materiel Command (W81XWH-05-1-0291) from 07/01/05 to 06/30/09.
- Tumor-targeted MR Contrast Enhancement Using Molecular Imaging Techniques. National Cancer Institute's Minority Institution/Cancer Center Partnership (MI/CCP) program Pilot Project Initiative.

Employment/Research Positions

Degrees Awarded:

- Dr. E. Chikezirim Agwu has submitted a Ph.D. thesis proposal.
- Mr. Armand Oei is going to attend professional school at the New England School of Optometry.

V. CONCLUSION

This is an extension of the 5th year of the training program. This program has supported four predoctoral students. One MD/PhD student has suffered an inherited Sickle Cell disease and has been hospitalized several times during the year. His PhD thesis work has been delayed. The PI has filed a second extension of this grant in order to continue supporting the student and the research. All the trainees have continued to learn the theory and instrumentation of MRI. The trainees have attended the weekly seminars in the Cancer Center and also attended a special NMR seminar series in the Department of Radiology. They are also actively involved in one of the four ongoing research projects. Three projects are continuation of previously reported projects. One project is new. It is to investigate the possibility using the molecular imaging technique to image amyloid plaques in the Alzheimer mouse brain. In this year, one paper has

been submitted to Molecular Imaging and it has been accepted for publication. Five abstracts have been presented in the national and international meetings. The PI has submitted two grant applications and received two new grants.

VI. REFERENCES

1. Brake GM, Karssemeijer N, Segmentation of suspicious densities in digital mammograms, Medical Physics, 2001, vol. 28, no. 2, pp. 259-266.
2. Heath M, Bowyer KW, Kopans D et al, Current status of the Digital Database for Screening Mammography, Digital Mammography, Kluwer Academic Publishers, 1998, pp. 457-460.
3. Li H, Wang Y, Liu KJR, Lo S-C, Freedman MT, Computerized Radiographic Mass Detection - Part I: Lesion Site Selection by Morphological Enhancement and Contextual Segmentation, IEEE Transactions on Medical Imaging, 2001, vol. 20, no. 4, pp. 289-301.
4. Mendez AJ, Tahoces PG, Lado MJ, Souto M., Vidal JJ, Computer-aided diagnosis: Automatic detection of malignant masses in digitized mammograms, Medical Physics, 1998, vol. 25, no. 6, pp. 957-964.
5. Sahiner B, Chan HP, Wei D, Petrick N, Helvie MA, Adler DD, Goodsit MM, Image feature selection by a genetic algorithm: Application to classification of mass and normal breast tissue, Medical Physics, 1996, vol.23, no.10, pp.1671-1684.
6. Balis FM, Drug interaction of commonly used anticancer drugs. Clin. Pharmacokin., 11, 223-235, 1986
7. Ibrahim S, Peggins J, Knapton A, Licht T, Aszalos A, Influence of beta-drenergic antagonists, H1-receptor blockers, analgesics, and quinolon antibiotics on the cellular accumulation of anticancer drug, daunorubicin: P-glycoprotein modulation. Anticancer Res., 21, 847-856, 2001
8. Gottesman MM, Fojo T and Bates SE, Multidrug resistance in cancer: role of ATP-dependent transporters. Nature Reviews, 2, 48-58, 2002
9. Schinkel A, Wagenar F, Mol C and Van Deemter L, P-glycoprotein in the blood-brain-barrier of mice influences the brain penetration and pharmacological activity of many drugs. J. Clin. Invest., 97,2517-2524, 1996
10. Tatsura T, Naito M, Ohhara T, Sugawara I and Tsuruo T, Functional involvment of P-glycoprotein in blood-brain-barrier. J. Biol. Chem., 267,20383-20391, 1992
11. Weissleder R, Mahmood U. Molecular Imaging. Radiology 219:316-333, 2001.
12. Sharma V, Luker GD, Piwnica-Worms D. Molecular imaging of gene expression and protein function *in vivo* with PET and SPECT. J Magn Reson Imag 16:336-351, 2002
13. Louise AY, Huber MM, Ahrens ET, Rothbacher U, Moats R, Jacobs RE, Fraser SE, Meade TJ. In vivo visualization of gene expression using magnetic resonance imaging. Nature Biotechnology 18:321-325, 2000.
14. Moore A, Basilion JP, Ciocca A, Weissleder R. Measuring transferrin receptor gene expression by NMR imaging. Biochemica Biophysica Acta 1402:239-249, 1998.
15. Artemov D, Mori N, Ravi R, Bhujwalla ZM, Magnetic resonance molecular imaging of the HER-2/neu receptor, Cancer Research 63: 2723-2727, 2003.

16. Xu L, Tang WH, Huang CC, Alexander W, Xiang LM, Pirollo KF, Rait A, Chang EH. Systemic p53 gene therapy of cancer with immunolipoplexes targeted by anti-transferrin receptor scFv. *Mol. Med.* 7:726-738, 2001.
17. Liang Xu, Cheng-Cheng Huang, Weiqun Huang, Wen-Hua Tang, Antonia Rait, Yu Zhi Yin, Idalia Criz, Lai-Man Xiang, Kathleen F. Pirollo, Ester H. Chang, Systemic tumor-targeted gene delivery by anti-transferrin receptor scFv-immunoliposomes. *Molecular Cancer Therapy*, 1:337-346, 2002.

VII. Appendices

Papers:

1. Kinnard L, Lo S-C.B, Wang PC, Freedman MT, Chouikha M, Separation of Malignant and Benign Masses Using Image and Segmentation Features. Proc. of SPIE, 2003 (This was listed as 'in press' in the 2003 annual report and it was not included in the 2004 annual report)
2. Kinnard L, Lo SB, Makariou E, Osicka T, Wang P, Chouikha MF, Freedman MT. Steepest changes of a probability-based cost function for delineation of mammographic masses: A validation study. Med. Phys. 31(10):2796-2810, 2004. (This was presented in 2004 Annual Report as a paper accepted for publication).
3. Pirollo K, Dagata J, Wang PC, Freedman M, Vladar A, Fricke S, Ileva L, Zhou Q, Chang EH. A Tumor-Targeted Nanodelivery System to Improve Early MRI Detection of Cancer. (Accepted for publication in *Molecular Imaging*).
4. Manaye KF, Wang, P, O'Neil J, Oei A, Song HF, Tizabi Y, Ingram DK, Mouton PR. MRI and Histological Correlations Of Cortical Brain Volumes In APP/PS1 Mice. (in preparation)

Abstracts:

1. Wang PC, Li E, Zhang R, Song H, Pirollo K, Chang EH. MR Image Enhancement by Tumor Cell Targeted Immunoliposome Complex Delivered Contrast Agent. Society for Molecular Imaging 3rd Annual Meeting, September 9-12, 2004, St. Louis, MO. (This was included in the 2004 Annual Report).
2. Manaye KF, Wang PC, O'Neil J, Oei A, Song H, Tizabi Y, Ingram DK, Mouton PR. In vivo and In vitro Stereological Analysis of Hippocampal and Brain Volumes in Young and Old APP/PS1 Mice Using Magnetic Resonance Neuroimages. Society of Neuroscience 34th Annual Meeting, October 23-27, 2004, San Diego, CA. (This was included in the 2004 Annual Report).
3. Wang PC, Aszalos A, Li E, Zhang R, Song HF, Malveaux R. Increased Transport of Trifluoperazine Across the Blood-Brain-Barrier Due to Modulation of P-glycoprotein. 9th RCMI International Symposium on Health Disparities. December 8-11, 2004, Baltimore, MD.
4. Agwu CL, Zhou J, Li E, Sridhar R, Wang PC. NMR Studies of Phosphorus Metabolites of Breast Cancer Cells Using An Improved Cell Perfusion System Applications for the Improved NMR Perfusion System for Breast Cancer Cell Study. 9th RCMI International Symposium on Health Disparities. December 8-11, 2004, Baltimore, MD.
5. Manaye KF, Wang PC, O'Neil J, Oei A, Song HF, Tizabi Y, Ingram DK, Mouton PR. In-Vivo and In-vitro Stereological Analysis of Hippocampal and Brain Volumes in Young and Old APP/PS1 Mice Using Magnetic Resonance Neuroimages. 9th RCMI International Symposium on Health Disparities. December 8-11, 2004, Baltimore, MD.

Separation of Malignant and Benign Masses Using Image and Segmentation Features

Lisa Kinnard^{a,b}, Shih-Chung B. Lo^a, Paul Wang^c, Matthew T. Freedman^a, Mohamed Chouikha^b

^aISIS Center, Dept. of Radiology, Georgetown University Medical Center, Washington, D.C.

^bDepartment of Electrical Engineering, Howard University, Washington, D.C.

^cBiomedical NMR Laboratory, Department of Radiology, Howard University, Washington, D.C.

ABSTRACT

The purpose of this study is to investigate the efficacy of image features versus likelihood features of tumor boundaries for differentiating benign and malignant tumors and to compare the effectiveness of two neural networks in the classification study: (1) circular processing-based neural network and (2) conventional Multilayer Perceptron (MLP). The segmentation method used is an adaptive region growing technique coupled with a fuzzy shadow approach and maximum likelihood analyzer. Intensity, shape, texture, and likelihood features were calculated for the extracted Region of Interest (ROI). We performed these studies: experiment number 1 utilized image features used as inputs and the MLP for classification, experiment number 2 utilized image features used as inputs and the neural net with circular processing for classification, and experiment number 3 used likelihood values as inputs and the MLP for classification. The experiments were validated using an ROC methodology. We have tested these methods on 51 mammograms using a leave-one-case-out experiment (i.e., Jackknife procedure). The A_z values for the four experiments were as follows: 0.66 in experiment number 1, 0.71 in experiment number 2, and 0.84 in experiment number 3.

Keywords: Computer-assisted diagnosis, breast cancer, convolution neural networks, feature extraction

1. INTRODUCTION

Many studies have investigated the efficacy of various features used in Computer-Assisted Diagnostic (CAD_x) systems. Sahiner et al.¹³ used texture and morphological features and used a genetic algorithm to select the best image features. In a study used to differentiate dense tissue from fatty tissue, Byng et al.¹ used fractal dimension and regional skewness as features. Qian et al.¹² calculated circularity, normalized deviation of radial length, intensity variation, mean intensity difference, and the mean gradient of region boundary. Wei et al.¹⁶ calculated the following eight texture features from the co-occurrence matrix: correlation, energy, entropy, inertia, inverse difference moment, sum average, sum entropy, and difference entropy. In a later study, Sahiner et al.¹⁵ calculated a Fourier descriptor, convexity, rectangularity, perimeter, Normalized Radial Length (NRL) mean, contrast, NRL entropy, circularity, NRL area ratio, NRL standard deviation, NRL zero crossing count, perimeter-to-area ratio, and area. These and other studies have been successful in finding features that are effective in separating from benign features, however, our study uses traditional features as well as segmentation features as inputs to two different classifiers.

In the United States, breast cancer accounts for one-third of all cancer diagnoses among women and it has the second highest mortality rate of all cancer deaths⁴. In various studies it has been shown that only 13% - 29% of suspicious lesions were determined to be malignant^{11, 13, 17} which indicates that there are high false positive rates for biopsied breast lesions. A higher predictive rate is anticipated by combining the mammographer's interpretation and the computer analysis. This could be of great clinical value because a lower amount of false positives in breast biopsies would reduce anxiety among patients and their families. Other studies show that 7.6-14% of the patients have mammograms that produce false negative diagnoses^{3, 8}. Alternatively, a CAD_x system can serve as a clinical tool for the radiologist and consequently lower the rate of missed breast cancer.

2. METHODOLOGY

The next several sections will describe the database, as well as provide the theoretical background used to develop the CAD_x experiment.

2.1 Database

The image samples were chosen from several databases compiled by the ISIS Center of the Georgetown University Radiology Department as well as the University of South Florida's (USF) Digital Database for Screening Mammography⁴. Twenty-eight malignant and twenty-three benign tumors were tested during this experiment.

2.2 Maximum Likelihood Segmentation Method

The segmentation method used in this study is an adaptive region growing technique coupled with a fuzzy shadow approach and maximum likelihood analyzer. The region growing technique aggregates surrounding pixels with similar properties, e.g., grayscale level. It is a commonly used method due to its simplicity and accuracy. The intensity threshold is usually used as a similarity criterion. We used the highest intensity as the seed point with multiple intensity threshold values and decreased the gray level in successive steps. This method by itself generated a sequence of contour on the mass; however, the computer did not have the ability to determine the boundaries interfered by other tissues and to choose the proper partition corresponding to the experts' perception. A fuzzy operator and a maximum-likelihood component were therefore added to the region-growing algorithm. The likelihood function is comprised of the likelihood of the composite probabilities for probability density functions (PDF's) inside ($p(S_i|pdf_i)$) and outside ($p(S_i|ROI)$) a given contour (see example contour in Figure 1)².

$$\text{Log}(P_i) = \log(p(S_i|pdf_i)) + \log(p(S_i|ROI)) \quad (1)$$

The subscript i represents the thresholding step, or, intensity value used to produce a given contour. The area inside the contour is the original ROI, which has been multiplied by a fuzzy shadow, whereas the area outside the contour is the original ROI. The likelihood that the contour represents the mass's extended borders is determined by assessing the maximum change of the likelihood function^{5,6}:

$$\arg \max \frac{d(\log(P_i))}{di} \quad (2)$$

To summarize, the best contour is determined by locating the steepest jump in likelihood values, i.e., the intensity corresponding to this location will produce the best contour.

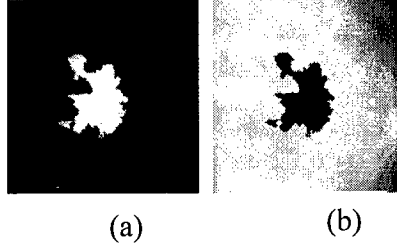


Figure 1: (a) ROI used to calculate $p(S_m|pdf_i)$. (b) ROI used to calculate $p(S_m|ROI)$ where m is the m^{th} contour corresponding to the maximum value of likelihood function indicated in eq. (2).

2.3 Feature Calculation

The features used to separate the malignant and benign masses were a combination of 18 statistical descriptors along with the likelihood features. The features have been separated into global features and sector features, where global features are those for which one value per mass is calculated. Sector features are those features calculated on the 10° ROI as it was divided into 10° sectors in the polar coordinate system (see **Figure 2**); therefore, each mass contained 36 sectors.

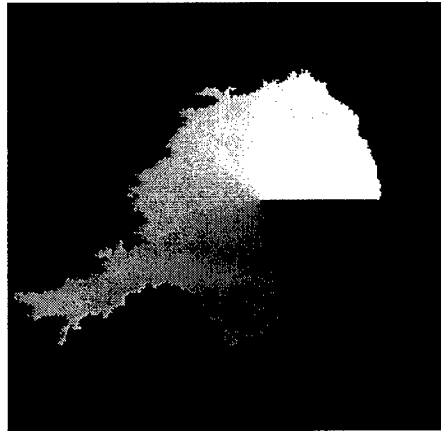


Figure 2: Sample map used to calculate sector features

In this study, three sets of features were used. One set of features is related to the use of the likelihood function curve which will be discussed in section 3. The other sets of features are as follows:

Global Features: skewness, kurtosis, circularity, compactness, and mass perimeter.

Local Features: mean intensity value, contrast, standard deviation inside the sector, sector area, deviation of the normalized radial length, radial length, roughness, energy, inertia, entropy, inverse difference moment, and difference entropy.

2.4 Classifiers

We used a conventional Multilayer Perceptron (MLP) neural network for two of the three studies described in this paper. The standard backpropagation training method was used for the MLP. It was comprised of an input layer, one hidden layer, and one output. We used a Multiple Circular Path Neural Network⁹ (MCPCNN) for the third study described in this paper (see **Figure 3**). It is comprised of 3 input layers, one hidden layer and one output. The first input layer is fully connected, i.e., all inputs connect to all hidden nodes. The second input layer is called a self correlation path, i.e., each node on the layer connects to a single set of the 18 image features for the fan-in and fully connects to the hidden nodes for fan-out. The third input layer is called a neighborhood correlation path, i.e., each node on the layer connects to the input nodes of adjacent sectors for the fan-in and fully connects to the hidden nodes for fan-out. Our study used 18 hidden layer nodes.

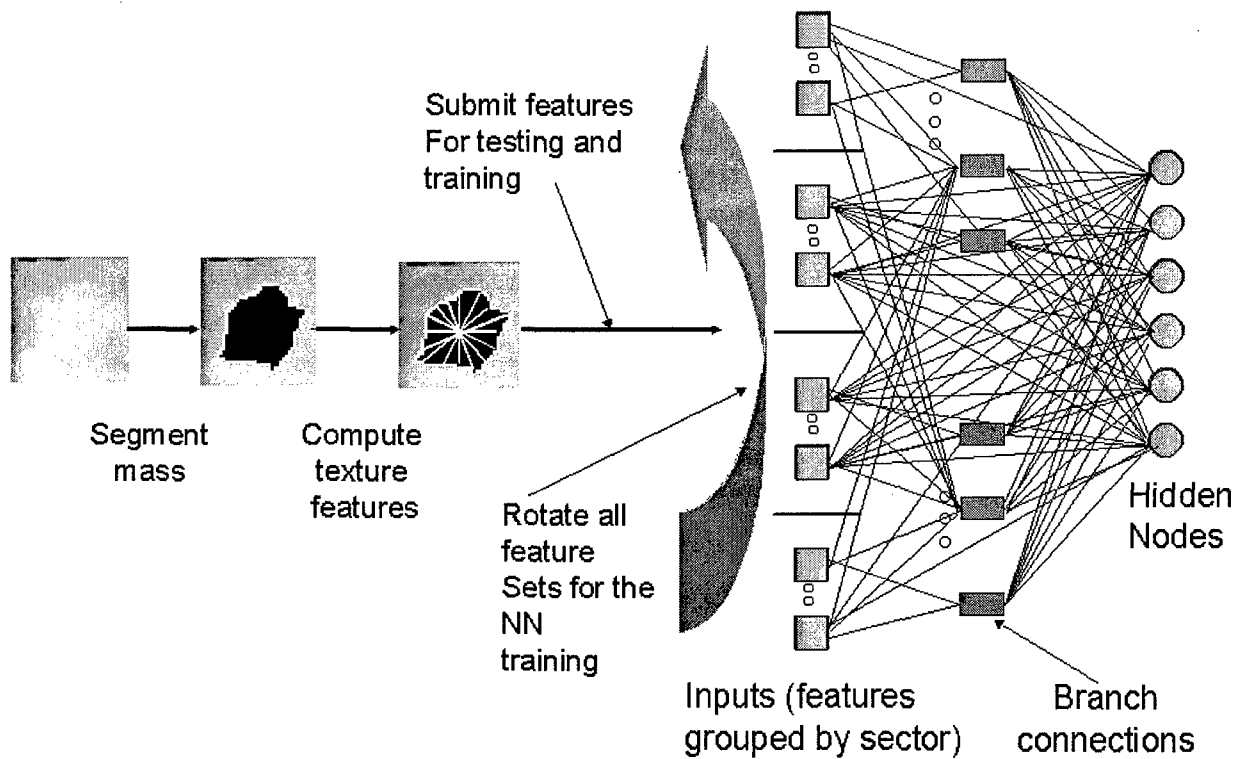


Figure 3: Multiple Circular Path Convolution Neural Network (MCPCNN)

3. EXPERIMENTS

In experiment 1 the input features consisted of 6 global image features combined with 12×36 sector image features to yield a total of 438 features. The classifier used for this experiment was a MLP neural network. It contained 18 hidden nodes and one output. Experiment 2 used the same image input features as those used in experiment 1, yet the classifier used for this experiment was the MCPCNN. The MCPCNN also contained 18 hidden nodes and one output. The neural networks were both tested and trained using the jackknife method. In experiment 3 the input values consisted of likelihood values that were extracted from the segmentation likelihood functions (see **Figures 5, 6**). The classifier used in this experiment was a MLP with 15 hidden nodes and one output. The neural network for this experiment was also tested and trained using the jackknife method. The results were analyzed using the LABROC4 analysis tool¹⁰. The experiments are summarized in **Table 1**.

4. RESULTS

The following table (**Table 1**) is a summary of the results achieved by the two classifiers used in the experiments described in section 2 of this paper. The corresponding ROC curves are shown in **Figure 4**. Two likelihood functions (features used in Experiment 3) along with their segmentation results (one malignant and one benign) are shown in **Figures 5 and 6**.

Table 1: Summary of Classification Results

Experiment	Features	Neural Network	A_z values
1	Image Features	MLP	0.66
2	Image Features	MCPCNN	0.71
3	ML-curve as features	MLP	0.84

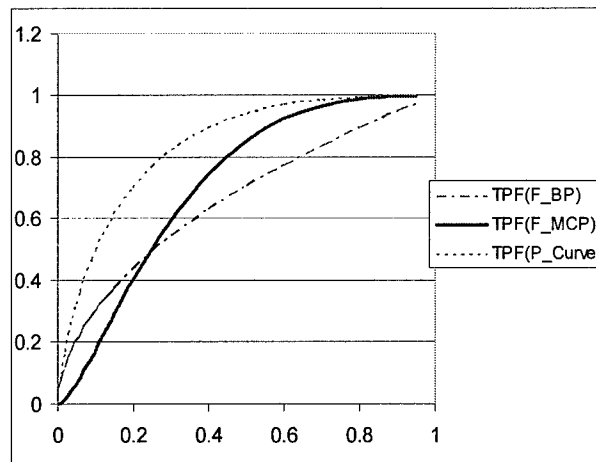
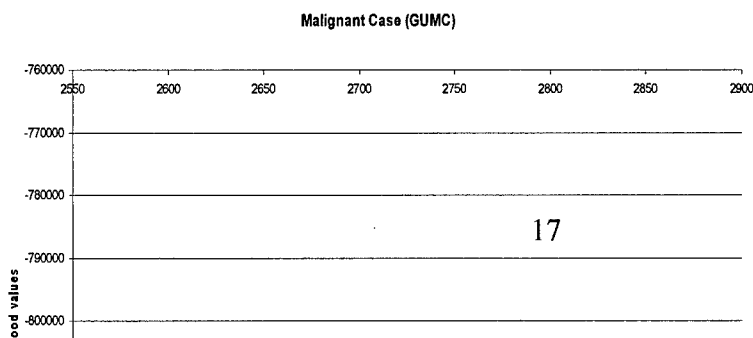


Figure 4: ROC Results (TPF: True Positive Fraction, F_BP: Experiment 1, F_MCP: Experiment 2, P_Curve: Experiment 3)



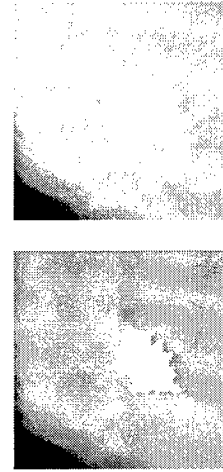


Figure 5: The segmentation results for a malignant tumor. (a) likelihood function with respect to threshold values for all segmentation steps (b) original image, (c) segmentation result

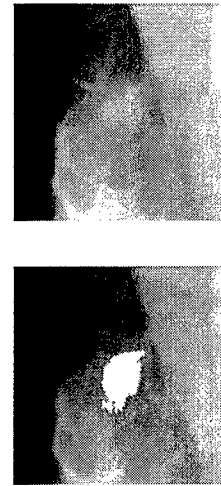
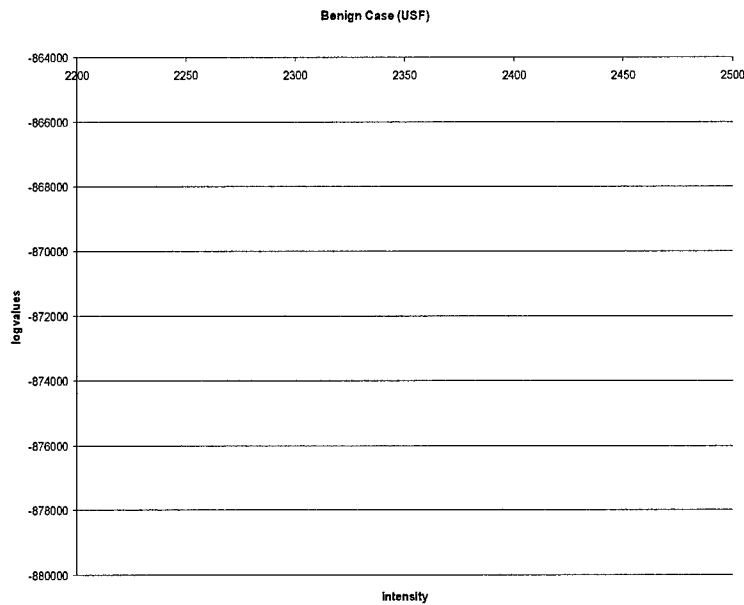


Figure 6: The segmentation results for a benign tumor. (a) likelihood function with respect to threshold values for all segmentation steps (b) original image, (c) segmentation result

5. DISCUSSION OF RESULTS

In general there is a marked difference between the shape of the likelihood function for benign cases and the likelihood function for malignant cases (see **Figures 5-6**, i.e., the likelihood

functions for benign cases experience a sharp drop and the likelihood functions for malignant cases are smoother, overall. In the image, a sharp drop in likelihood value represents an abrupt change in segmented area.

Overall MCPCNN performed better (see **Figure 4**) than the conventional neural network, where the A_z value for Experiment 1 was 0.66, the A_z value for Experiment 2 was 0.71 and the A_z value for Experiment 3 was 0.84. The likelihood functions used as features provided the best diagnostic results, with regard to neural network performance. We believe that this phenomenon occurred because there is a clear difference between the appearance of the benign likelihood functions and the malignant likelihood functions. This may not be the case with regard to image features as some benign masses have malignant characteristics (e.g. - ill-defined borders) and vice versa. In future work we plan to find likelihood functions for various sectors, because we believe that certain sectors hold more valuable information than others. If we combine the feature information with likelihood functions found in the various sectors and use the MCPCNN, we could improve the performance in the classification of mammographic masses.

6. CONCLUSION

We found that the maximum likelihood method in conjunction with fuzzy shadow approach is an effective approach for not only segmenting masses, but for also using its results to separate malignant and benign masses. Our method includes a fully-automated segmentation technique as well as the use of sector features that are designed for the separation of malignant and benign masses. We have also shown that the Multiple Circular Path Convolution Neural Network is better at separating malignant from benign masses and that the best classifier performance is achieved when the maximum likelihood features are used as inputs.

ACKNOWLEDGMENTS

This work was support by US Army Grant numbers DAMD17-00-1-0291 and DAMD17-01-1-0267. The content of this paper does not necessarily reflect the position or policy of the government.

REFERENCES

1. Byng JW, Boyd NF, Fishell E, Jong RA, Yaffe MJ, Automated analysis of mammographic densities, *Physics in Medicine and Biology*, 1996, vol. 41, pp. 909-923.
2. Comer ML, Liu S, Delp EJ, Statistical Segmentation of Mammograms, *Proceedings of the 3rd International Workshop on Digital Mammography*, Chicago, IL, June 9-12, 1996, pp. 475-478.
3. Harvey JA, Fajardo LL, Innis, CA, Previous Mammograms in Patients with Impalpable Breast Carcinoma: Retrospective vs. Blinded Interpretation, *American Journal of Roentgenology*, 1993, vol. 161, pp. 1167-1172.
4. Heath M, Bowyer KW, Kopans D et al, Current status of the Digital Database for Screening Mammography}, *Digital Mammography*, Kluwer Academic Publishers, 1998, pp. 457-460.
5. Kinnard L, Lo S-C B, Wang P, Freedman MT, Chouikha M, Separation of Malignant and Benign Masses using a Maximum-Likelihood Analysis and Neural Networks, *Proceedings of the SPIE Medical Imaging Conference*, February, 2002, vol. 4684, part II, pp. 733-741.

6. Kinnard L, Lo S-C B, Wang P, Freedman MT, Chouikha M, Automatic Segmentation of Mammographic Masses Using Fuzzy Shadow and Maximum-Likelihood Analysis, Proceedings of the International Symposium on Biomedical Imaging (ISBI), July, 2002, pp. 241-244.
7. Lacey JV Jr, Devesa SS, Brinton LA, Recent trends in breast cancer incidence and mortality, 2002, vol. 39, no.2-3, pp. 82-88.
8. Martin JE, Moskowitz M, Milbrath JR, Breast Cancer Missed by Mammography, American Journal of Roengenology, 1979, vol. 132, pp. 737-739.
9. Lo SC, Li H, Wang J, Kinnard L, Freedman MT, A Multiple Circular Path Convolution Neural Network System for Detection of Mammographic Masses, IEEE Transactions on Medical Imaging, 2002, vol. 21, No. 2, pp. 150-158.
10. Metz C, LABROC Program, <ftp://radiology.uchicago.edu/roc>.
11. Meyer JE, Kopans DB, Stomper PC, Lindfors KK, Occult Breast Abnormalities: Percutaneous Preoperative Needle Localization, Radiology, 1984, vol. 150, no. 2, pp. 335-337.
12. Qian W, Li L, Clarke LP, Image feature extration for mass detection in digital mammography: Influence of wavelet analysis, 1999, Medical Physics, vol. 26, no. 3, pp. 402-408.
13. Rosenberg AL, Schwartz GF, Feig SA, Patchefsky AS, Clinically Occult Breast Lesions: Localization and Significance, Radiology, 1987, vol. 162, no. 1, pp. 167-170.
14. Sahiner B, Chan H-P, Wei D, Petrick N, Helvie MA, Adler DD, Goodsitt MM, Image feature selection by a genetic algorithm: Application to classification of mass and normal breast tissue, Medical Physics, 1996, vol. 23, no. 10, pp. 1671-1684.
15. Sahiner B, Chan H-P, Petrick N, Helvie MA, Hadjiiski LM, Improvement of mammographic mass characterization using spiculation measures and morphological features, Medical Physics, 2001, vol.28, no. 7, pp. 1455-1465.
16. Wei D, Chan H-P, Helvie MA, Sahiner B, Petrick N, Adler DD, Goodsitt MM, False-positive reduction technique for detection of masses on digital mammograms: Global and local multiresolution texture analysis, Medical Physics, 1997, vol. 24, no. 6, pp. 903-914.
17. Yankaskas BC, Knelson MH, Abernethy ML, Cuttino JT, Clark RL, Needle Localization Biopsy of Occult Lesions of the Breast, vol. 23, no. 10, pp. 729-733.

Steepest changes of a probability-based cost function for delineation of mammographic masses: A validation study

Lisa Kinnard

*ISIS Center, Georgetown University Medical Center, Washington, DC 20057-1479,
Department of Electrical and Computer Engineering, Howard University, Washington, DC,
and Biomedical NMR Laboratory, Department of Radiology, Howard University, Washington, DC*

Shih-Chung B. Lo^{a)}

ISIS Center, Georgetown University Medical Center, Washington, DC 20057-1479

Erini Makariou

ISIS Center, Georgetown University Medical Center, Washington, DC 20057-1479

Teresa Osicka

*ISIS Center, Georgetown University Medical Center, Washington, DC 20057-1479
and Department of Electrical Engineering and Computer Science, The Catholic University of America,
Washington, DC*

Paul Wang

Biomedical NMR Laboratory, Department of Radiology, Howard University, Washington, DC

Mohamed F. Chouikha

Department of Electrical and Computer Engineering, Howard University, Washington, DC

Matthew T. Freedman

ISIS Center, Georgetown University Medical Center, Washington, DC 20057-1479

(Received 5 January 2004; revised 16 April 2004; accepted for publication 22 June 2004;
published 17 September 2004)

Our purpose in this work was to develop an automatic boundary detection method for mammographic masses and to rigorously test this method via statistical analysis. The segmentation method utilized a steepest change analysis technique for determining the mass boundaries based on a composed probability density cost function. Previous investigators have shown that this function can be utilized to determine the border of the mass body. We have further analyzed this method and have discovered that the steepest changes in this function can produce mass delineations that include extended projections. The method was tested on 124 digitized mammograms selected from the University of South Florida's Digital Database for Screening Mammography (DDSM). The segmentation results were validated using overlap, accuracy, sensitivity, and specificity statistics, where the gold standards were manual traces provided by two expert radiologists. We have concluded that the best intensity threshold corresponds to a particular steepest change location within the composed probability density function. We also found that our results are more closely correlated with one expert than with the second expert. These findings were verified *via* Analysis of Variance (ANOVA) testing. The ANOVA tests obtained *p*-values ranging from 1.03×10^{-2} – 7.51×10^{-17} for the single observer studies and 2.03×10^{-2} – 9.43×10^{-4} for the two observer studies. Results were categorized using three significance levels, i.e., $p < 0.001$ (extremely significant), $p < 0.01$ (very significant), and $p < 0.05$ (significant), respectively. © 2004 American Association of Physicists in Medicine. [DOI: 10.1118/1.1781551]

Key words: mass boundary detection, mammography, probability-based cost function

I. INTRODUCTION

In the United States, breast cancer accounts for one-third of all cancer diagnoses among women and it has the second highest mortality rate of all cancer deaths in women.¹ Breast cancer studies are therefore essential for its ultimate eradication. Several studies show that only 13%–29% of suspicious masses are determined to be malignant,^{2–4} indicating that there are high false positive rates for biopsied breast masses. A higher predictive rate is anticipated by combining the mammographer's interpretation and the computer analysis.

Other studies show that 7.6%–14% of the patients have mammograms that produce false negative diagnoses.^{5,6} Alternatively, a Computer Assisted Diagnosis (CAD_x) system can serve as a clinical tool for the radiologist and consequently lower the rate of missed breast cancer.

Generally, CAD_x systems consist of three major stages, namely, segmentation, feature calculation, and classification. Segmentation is arguably one of the most important aspects of CAD_x—particularly for masses—because a strong diagnostic predictor for masses is shape. Specifically, many ma-

lignant masses have ill-defined, and/or spiculated borders and many benign masses have well-defined, rounded borders. Furthermore, breast masses can have unclear borders and are sometimes obscured by glandular tissue in mammograms. During the search for suspicious areas masses of this type may be overlooked by radiologists. When a specific area is deemed to be suspicious, the radiologist analyzes the overall mass, including its shape and margin characteristics. The margin of a mass is defined as the interface between the mass and surrounding tissue, and is regarded by some as one of the most important factors in determining its significance.⁷ Specifically, a spiculated mass consists of a central mass body surrounded by fibrous extensions, hence the resulting stellate shape. In this context, "extension" refers to those portions of the mass containing ill-defined borders, spiculations, fibrous borders, and projections. Although the diameters of these cancers are measured across the central portion of the mass, microscopic analysis of the extensions also reveals associated cancer cells, in other words, the extended projections may contain active mass growth.^{7,8} In addition, the features of the extended projections and ill-defined borders are highly useful for identifying masses. Hence, proper segmentation—including the body and periphery—is essential for the computer to analyze, and in turn, determine the malignancy of the mass in mammographic CAD_x systems.

Te Brake and Karssemeijer⁹ implemented a discrete dynamic contour model, a method similar to snakes, which begins as a set of vertices connected by edges (initial contour) and grows subject to internal and external forces. Li¹⁰ developed a method that employs *k*-means classification to categorize pixels as belonging to the region of interest (ROI) or background. Petrick *et al.*¹¹ developed the Density Weighted Contrast Enhancement (DWCE) method, in which series of filters are applied to the image in an attempt to extract masses. Pohlman *et al.*¹² developed an adaptive region growing method whose similarity criterion is determined from calculations made in 5×5 windows surrounding the pixel of interest. Mendez *et al.*¹³ developed a method, which combined bilateral image subtraction and region growing.

Several studies have also used probability-based analysis to segment digitized mammograms. Li *et al.*¹⁴ developed a segmentation method that first models the histogram of mammograms using a finite generalized Gaussian mixture (FGGM) and then uses a contextual Bayesian relaxation labeling (CBRL) technique to find suspected masses. Furthermore, this method uses the Expectation-Maximization (EM) technique in developing the FGGM model. Comer *et al.*¹⁵ utilized an EM technique to segment digitized mammograms into homogeneous texture regions by assigning each pixel to one of a set of classes such that the number of incorrectly classified pixels was minimized. Kupinski and Giger¹⁶ developed a method, which combines region growing with probability analysis to determine final segmentation. In their method, the probability-based function is formed from a specific composed probability density function, determined by a set of image contours produced by the region growing method. This method is a highly effective one and it was

implemented by Te Brake and Karssemeijer in their work⁹ that compared the results of a model of the discrete dynamic contour model with those of the probability-based method. For this reason, we chose to investigate its use as a possible starting point from which a second method could be developed. Consequently for our implementation of this work we discovered an important result, i.e., the steepest changes of a cost function composed from two probability density functions of the regions. It appears that in many cases this result produces contour choices that encapsulate important borders such as mass spiculations and ill-defined borders.

Several CAD_x classification techniques have been developed. They are described here to underscore the importance of accurate segmentation in CAD_x studies. Lo *et al.*¹⁷ developed an effective analysis method using the circular path neural network technique that was specifically designed to classify the segmented objects, and it can certainly be extended for the applications related to mass classification. Polakowski *et al.*¹⁸ used a multilayer perceptron (MLP) neural network to distinguish malignant and benign masses. Both Sahiner *et al.*¹⁹ and Rangayyan *et al.*²⁰ used linear discriminant analysis to distinguish benign masses from malignant masses. While many CAD_x systems have been developed, the development of fully-automated image segmentation algorithms for breast masses has proven to be a daunting task.

II. METHODS

A. Segmentation method—Maximum change of cost function as a continuation of probability-based function analysis

As a point of clarification, the function used to find optimal region growing contours in the Kupinski and Giger study¹⁶ is referred to as the probability-based function and our function is referred to as the cost function. The two functions are similar, however they differ in terms of the images used in their formation. As an initial segmentation step, the region growing is used to aggregate the area of interest,^{12,13,21} where grayscale intensity is the similarity criterion. This phase of the algorithm starts with a seed point whose intensity is high, and nearby pixels with values greater than or equal to this value are included in the region of interest. As the intensity threshold decreases, the region increases in size, therefore there is an inverse relationship between intensity value and contour size. In many cases the region growing method is extremely effective in producing contours that are excellent delineations of mammographic masses. However, the computer is not able to choose the contour that is most highly correlated with the experts' delineations, specifically, those masses that contain ill-defined margins or margins that extend into surrounding fibroglandular tissue. Furthermore, the task of asking a radiologist to visually choose the best contour would be both time intensive and extremely subjective from one radiologist to another.

The segmentation technique described in this work attempts to solve and automate this process by adding a two-dimensional (2-D) shadow and probability-based compo-

nents to the segmentation algorithm. Furthermore, we have devised a steepest descent change analysis method that chooses the best contour which delineates the mass body contour as well as its extended borders, i.e., extensions into spiculations and areas in which the borders are ill-defined or obscured. It has been discovered that the probability-based function is capable of extracting the central portion of the mass density as demonstrated by the previous investigators,¹⁶ and in this work the method has been advanced further such that it can include the extensions of the masses. The enhanced method can produce contours, which closely match expert radiologist traces. Specifically, it has been observed that this technique can select the contour that accurately represents the mass body contour for a given set of parameters. However, a further analysis of the cost function composed from the probability density functions inside and outside of a given contour revealed that the computer could choose a set of three segmentation contour choices from the entire set of contour choices, and latter make a final decision from these three choices.

1. Region growing and preprocessing

Initially, a 512×512 pixel area surrounding the mass was cropped. The region growing technique^{12,13,21} to aggregate the region of interest was employed, where the similarity criterion for our region growing algorithm is grayscale intensity. To start the growth of the first region, a seed point was placed at the center of the 512×512 ROI. The region growing process continues by decreasing the intensity value until we have grown a sufficiently large set of contours.

Next, the image is multiplied by a 2-D trapezoidal membership function with rounded corners whose upper base measures 40 pixels and lower base measures 250 pixels (1 pixel = 50 microns). This function was chosen because it is a good model of the mammographic mass' intensity distribution. Since the ROI's have been cropped such that the mass' center was located at the center of the $512 \text{ pixel} \times 512 \text{ pixel}$ area, shadow multiplication emphasizes pixel values at the center of the ROI and suppresses background pixels. The image to which the shadow has been applied is henceforth referred to as the "processed" image. The original image and its processed version were used to compute the highest possibility of its boundaries. The computation method is comprised of two components for a given boundary: (1) formulation of the composed probability as a cost function and (2) evaluation of the cost function.

The contours were grown using the original image as opposed to the processed image, and this choice accounts for a major difference between the current implementation and that of the previous investigators.¹⁶ By using contours generated from the original image, a cost function composed from the probability density functions inside and outside of the contours was produced. In many situations, the greatest changes in contour shape and size occur at sudden decreases within the function. In analyzing these steep changes it was observed that the intensity values corresponding to the steep changes typically produced contours that encapsulated both

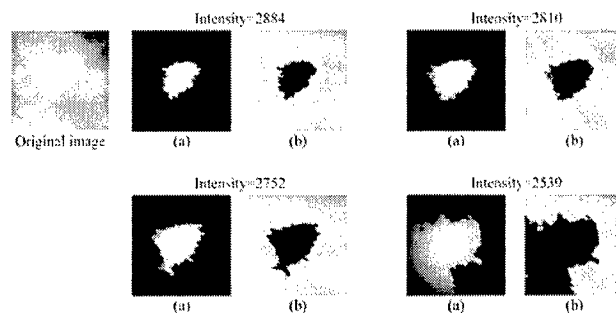


FIG. 1. Four grown contours used to construct the cost function: starts from high intensity thresholds and moves towards low intensity thresholds. Each contour separates the ROI into two parts: (a) Segmented image (based on processed image) used to compute density function $p(f_i(x,y)|S_i)$ and (b) masked image (based on the nonprocessed original image) used to compute density function $p(m_i(x,y)|S_i)$ for four intensity threshold values.

the mass body as well as its spiculated projections or ill-defined margins. This phenomenon would be suppressed if the processed image was used to generate the contour. A more detailed discussion of steep changes within the cost function is forthcoming in Sec. II A 2 C.

The processed image was mainly used to construct the cost function. A common technique used in mass segmentation studies is to pre-process the images using some type of filtering mechanism^{11,16} in an effort to separate the mass from surrounding fibroglandular tissue. This method could be particularly beneficial to the region growing process because it would aid in preventing the regions from growing into surrounding tissue. Alternatively, the filtering process could impede our goal of attempting to encapsulate a mass's extended borders as well as borders that are ill-defined due to the filtering process's tendency to create rounded edges on margins that are actually jagged or spiculated. This phenomenon could potentially defeat the goal of extracting mass borders. For these reasons, we have chosen to aggregate the contours using the original ROI rather its processed version.

2. Formulation of the composed probability as a cost function

In the context of this work, the composed probability is defined as the probability density functions of the pixels inside and outside a contour using a processed and nonprocessed version of an image. Specifically, for a contour (S_i), the composed probability (C_i) is calculated:

$$C_i|S_i = \prod_{j=0}^h p(f_i(x,y)|S_i) \times \prod_{j=0}^h p(m_i(x,y)|S_i). \quad (1)$$

The quantity $f_i(x,y)$ is the set of pixels, which lie inside the contour S_i [see Fig. 1(a)], and this area contained processed pixel values. The quantity $p(f_i(x,y)|S_i)$ is the probability density function of the pixels inside S_i ($f_i(x,y)$), where "i" is the intensity threshold used to produce the contours given by the region growing step, and "h" is the maximum intensity value. The quantity $m_i(x,y)$ is the set of pixels, which lie outside the contour S_i [see Fig. 1(b)], and this area contained nonprocessed pixels. The quantity $p(m_i(x,y)|S_i)$ is

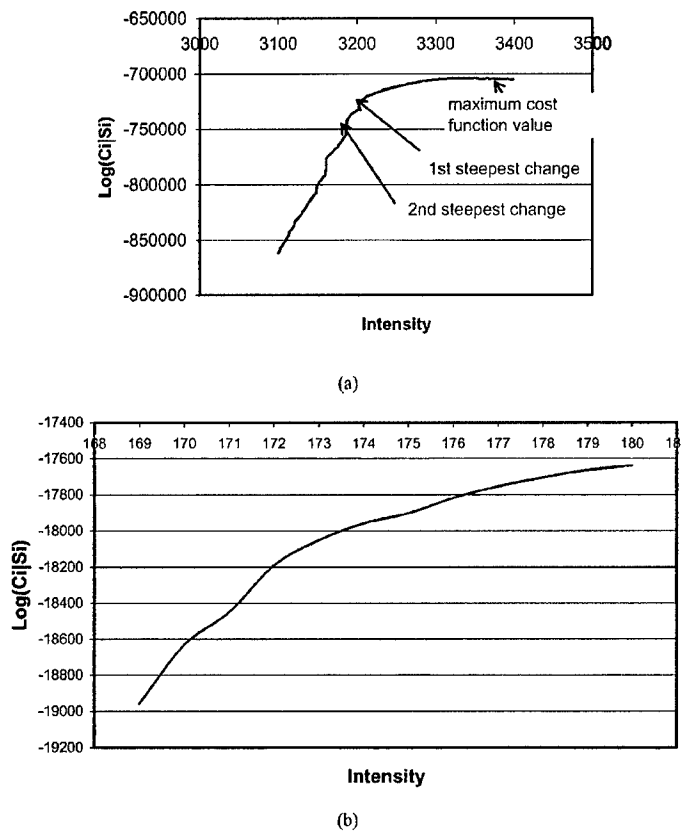


FIG. 2. (a) Example of cost function with steepest change location indicators. (b) Example of a probability-based function without an obvious steepest change location.

the probability density function of the pixels outside S_i , where “ i ” is the intensity threshold used to produce the contours given by the region growing step, and “ h ” is the maximum intensity value. For implementation purposes, the logarithm of the composed probability of the two regions, C_i was used:

$$\begin{aligned} \text{Log}(C_i|S_i) = & \log\left(\prod_{j=0}^h p(f_i(x,y)|S_i)\right) \\ & + \log\left(\prod_{j=0}^h p(m_i(x,y)|S_i)\right). \end{aligned} \quad (2)$$

3. The cost function based on the composed probability density functions

To select the contour that represents the fibrous portion of the mass, it is appropriate to examine the maximum value of the cost function:

$$\arg \max(\text{Log}(C_i|S_i); S_i, i = 1, \dots, n). \quad (3)$$

It has been assessed (also by other investigators^{9,16}) that the intensity value corresponding to this maximum value is the optimal intensity needed to delineate the mass body contour. However, in the current implementation it was discovered that the intensity threshold corresponding to the maximum value confines the contour to the fibrous portion of the mass, or, the mass body. In this study many of these contours did not include the extended borders. It is therefore hypothesized that the contour representing the mass extended borders may

well be determined by assessing the greatest changes of the cost function, or locating the steepest value changes within the function

$$\frac{d}{di} (\text{Log}(C_i|S_i); S_i, i = 1, \dots, n). \quad (4)$$

Based on this assumption, cost functions associated with masses were analyzed. The analysis reveals that the most likely boundaries of masses associated with expert radiologist traces are usually produced by the intensity value corresponding to the first or second steepest change of value immediately following the maximum value on the cost function [see Fig. 2(a)]. The description of this discovery is given below. It is followed by a validation study described in Sec. II B and by results shown in Sec. III. The overarching goal of the steep descent method is to determine whether a certain contour is the best contour, and whether it represents the mass and its extended borders.

4. The definition of steepest change

The term “steepest change” is rather subjective. In this work we define it as a location between two or more points in the cost function where the values experience a significant change. When the values are plotted as a function of intensity, these significant changes are often visible in the function. In some cases the cost function increases at a slow rate, therefore a potential steepest change location could be missed. The algorithm design compensates for this issue by

calculating the difference between values in steps over several values and comparing the results to two threshold values. The difference equation is given by

$$d(t) = f(z - wt) - f(z - w(t + 1)), \quad t = 0, m, \quad (5)$$

where f is the cost function, z is the maximum intensity, w is the width of the interval over which the cost function differences are calculated (e.g., for $w = 5$ differences are calculated every 5 points), and m is the total number of points in the searchable area divided by w . Note that " wt " is associated with a specific contour " i " described earlier. If the value of $d(t)$ yields a value greater than or equal to a given threshold, then the intensity corresponding to this location is determined to be a steepest change location. The threshold algorithm occurs as follows:

If $(d(t) \geq TV_1); \quad t = 0, \dots, m$

Then choice 1 = intensity where that condition is satisfied.

If $(d(t) \geq TV_2); \quad t = m, \dots, z$

Then choice 2 = intensity where that condition is satisfied.

where TV_1 and TV_2 are pre-defined threshold values, m is the location in the function where the choice 1 condition is satisfied, and z is the location in the function where the choice 2 condition is satisfied. During the examination of the contour growth with respect to the cost function, the first steepest change [$d(t)_{MC1}$ as choice 1] is determined by TV_1 immediately after the location of the maximum cost function value (corresponding to the mass body discussed earlier). The second the steepest change [$d(t)_{MC2}$ as choice 2] is determined by TV_2 after the first steepest change has been established.

Figure 1(a) illustrates how the algorithm is carried out. In this figure, the maximum value on the cost function occurs for a grayscale intensity value of approximately 3330. The searching process begins from this maximum point and it is discovered that the first steepest change [$d(t)_{MC1}$ as choice 1] occurs for a grayscale intensity value approximately equal to 3200. From this point the searching process continues and it is discovered that the second steepest change [$d(t)_{MC2}$ as choice 2] occurs for a grayscale intensity value approximately equal to 3175. In summary, intensity values of 3330, 3200, and 3175 can be used to grow 3 potential mass delineation candidates, and the large set of intensity choices has been narrowed to 3 choices. The following scenarios occurred when the three contour choices produced by the (1) maximum intensity value on the cost function (2) the intensity corresponding to the first steepest change on the cost function, and (3) the intensity corresponding to the second steepest change on the cost function.

(1) Intensity corresponding to the maximum value on the cost function: The central body of the mass was encapsulated.

- (2) Intensity corresponding to the first steepest change on the cost function: The central body of the mass + some of its extended borders (i.e., projections and spiculations) was encapsulated.
- (3) Intensity corresponding to the second steepest change on the cost function: The central body of the mass + more extended borders + surrounding fibroglandular tissue was encapsulated.

The intensity corresponding to the first steepest change provides the best choice, and an examination of this observation is shown and discussed in Secs. III and IV of this work.

As stated previously, the steep changes within the cost function would be suppressed if the processed image was used to generate the contour; therefore, the function would be relatively smooth. Figure 2(b), which shows a probability-based function produced by contours that were grown using a processed ROI, demonstrates this issue.

B. Validation method

In several segmentation studies the results were validated using the overlap statistic alone, however, it was necessary to analyze the performance of the steepest change algorithm on the basis of four statistics to verify that the algorithm is indeed capable of categorizing mass and background pixels correctly. This type of analysis provides helpful information regarding necessary changes for the algorithm's design and can possibly aid in its optimization.

The segmentation method was validated on the basis of overlap, accuracy, sensitivity, and specificity.^{22,23} These statistics are calculated as follows:

$$\text{Overlap} = \frac{N_{TP}}{N_{FN} + N_{TP} + N_{FP}}, \quad (6)$$

$$\text{Accuracy} = \frac{N_{TP} + N_{TN}}{N_{TP} + N_{TN} + N_{FP} + N_{FN}}, \quad (7)$$

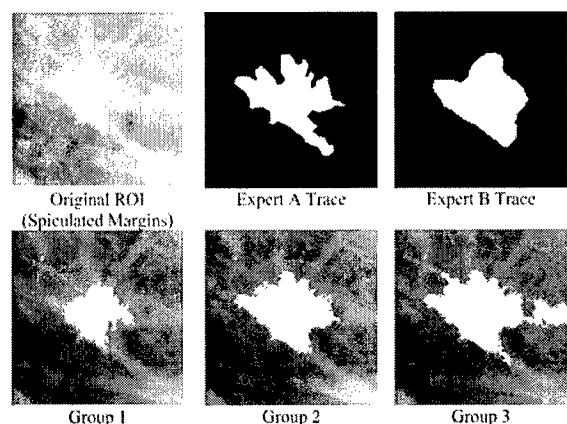
$$\text{Sensitivity} = \frac{N_{TP}}{N_{TP} + N_{FN}}, \quad (8)$$

$$\text{Specificity} = \frac{N_{TN}}{N_{TN} + N_{FP}}, \quad (9)$$

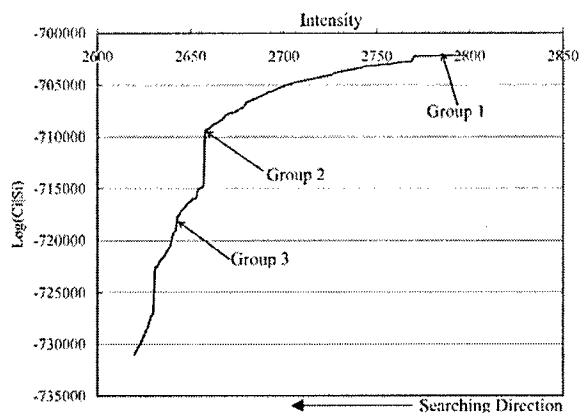
where N_{TP} is the true positive fraction (part of the image correctly classified as mass), N_{TN} true negative fraction (part of the image correctly classified as surrounding tissue), N_{FP}

TABLE I. Distribution of DDSM masses studied according to their subtlety ratings.

Subtlety category	Cancer	Benign
Number of masses with a rating=1	5	3
Number of masses with a rating=2	12	12
Number of masses with a rating=3	18	17
Number of masses with a rating=4	9	23
Number of masses with a rating=5	15	10



(a)

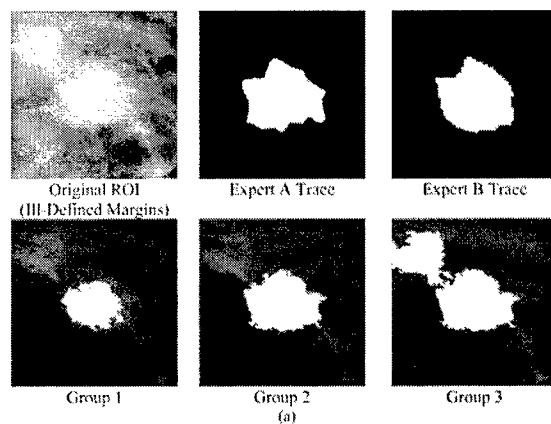


(b)

FIG. 3. (a) Segmentation results for a malignant mass with spiculated margins (subtlety=2) (b) the corresponding cost function.

is the false positive fraction (part of the image incorrectly classified as mass), and N_{FN} is the false negative fraction (part of the image incorrectly classified as surrounding tissue). This method requires a gold standard, or, a contour to which the segmentation results can be compared. The gold standards for the experiments performed in this work were mass contours, which have been traced by expert radiologists.

The experiments produced contours for the intensity values resulting from three locations within the cost functions: (1) The intensity of the maximum value within the cost function; (2) the intensity for which the cost function experiences its first steepest change; and (3) the intensity for which the cost function experiences its second steepest change. It has been observed that the intensity for which the cost function experiences its first steepest change produces the contour trace that is most highly correlated with the gold standard traces, regarding overlap and accuracy. In cases for which better results occur at the second steepest change location, there is no significant difference between these results and the results calculated for the first steepest change location. Second, it has been observed that the results are more closely correlated with one expert than with the second expert. These hypotheses were tested using the one-way Analysis of Vari-



(a)

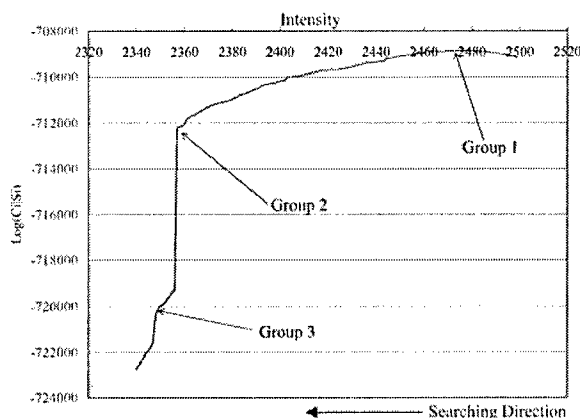


FIG. 4. (a) Segmentation results for a malignant mass with ill-defined margins (subtlety=3); (b) the corresponding cost function.

ance (ANOVA) test.^{24,25} In this study, three significance levels (i.e., $p < 0.001$, $p < 0.01$, and $p < 0.05$) were used to categorize the ANOVA results as described in the next section.

III. EXPERIMENTS AND RESULTS

The following sections describe the database and experiments, and provide segmentation results and ANOVA test results.

A. Database

For this study, a total of 124 masses were chosen from the University of South Florida's Digital Database for Screening Mammography (DDSM).²⁶ The DDSM films were digitized at 43.5 or 50 μm 's using either the Howtek or Lumisys digitizers, respectively. The DDSM cases have been ranked by expert radiologists on a scale from 1 to 5, where 1 represents the most subtle masses and 5 represents the most obvious masses. Table I lists the distribution of the masses studied according to their subtlety ratings. The images were of varying contrasts and the masses were of varying sizes.

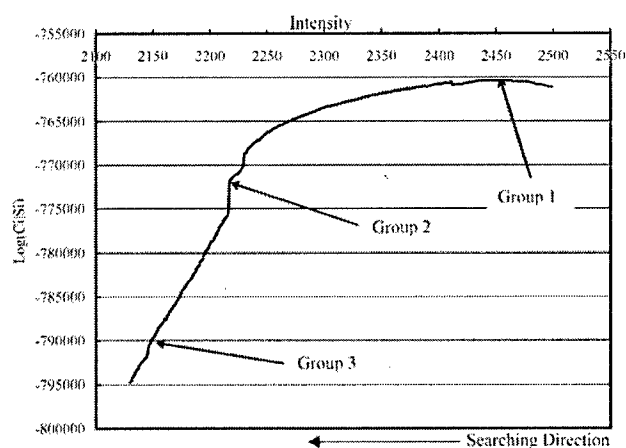
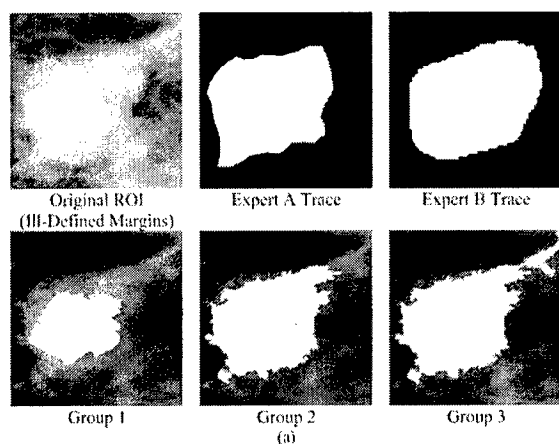


FIG. 5. (a) Segmentation results for a benign mass with ill-defined margins (subtlety=3); (b) the corresponding cost function.

The first set of expert traces was provided by an attending physician at Georgetown University Medical Center (GUMC), and is hereafter referred to as the Expert A traces. The second set of expert traces was provided by the DDSM, and is hereafter referred to as the Expert B traces.

B. Experiments

As mentioned previously, the term “steepest change” is very subjective. Therefore, a set of thresholds needed to be set in an effort to define a particular location within the cost function as a “steepest change location.” For this study the following thresholds were experimentally chosen: $TV_1 = 1800$, $TV_2 = 1300$, where TV_1 equals the threshold for steepest change location 1 for the cost function, and TV_2 equals the threshold for steepest change location 2 for the cost function. A number of experiments were performed in an effort to prove that (1) the intensity for which the cost function experiences the first steepest change location produces the contour trace, which is most highly correlated with the gold standard traces with regard to overlap and accuracy. In cases for which the second steepest change location achieves better results, there are no significant differences between the values obtained from the first steepest change

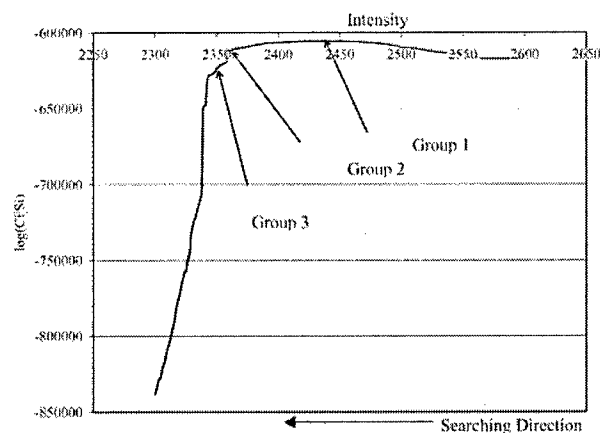
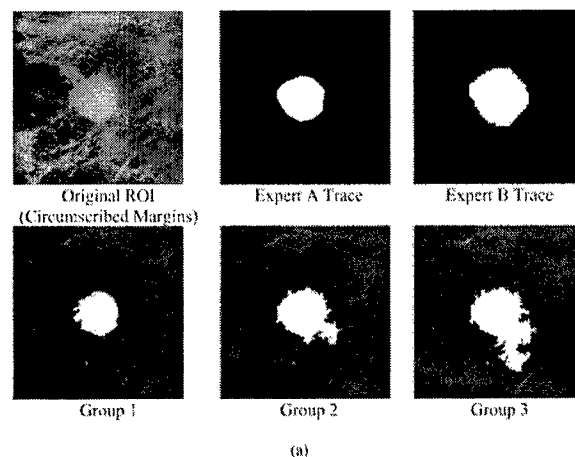


FIG. 6. (a) Segmentation results for a benign mass with circumscribed margins (subtlety=4); (b) the corresponding cost function.

location and the second steepest change location. The experiments linked with these hypotheses comprise the studies for a single observer. We have also set out to prove that (2) our results are more closely correlated with one expert than with the second expert. The experiments linked with this hypothesis comprise the studies between two observers. First segmentation results for two malignant cases are presented, followed by segmentation results for two benign cases. Second, the ANOVA results for a set of hypotheses are presented. The contours produced by the maximum value as well as by the steepest change locations within the cost functions are labeled as follows: (1) group 1: The intensity for which a value within the cost function is maximum; (2) group 2: The intensity for which the cost function experiences its first steepest change; (3) group 3: The intensity for which the cost function experiences its second steepest change.

C. Results

Figures 3–6 display the results for two malignant cases accompanied by their cost functions as well as results for two benign cases accompanied by their cost functions. The ANOVA results appear in a set of tables (Secs. II–IV), where each table lists the hypothesis tested along with p -values and their corresponding categorizations. The p -values are catego-

rized in the following way: not significant (NS for $p > 0.05$), significant (S for $p < 0.05$), very significant (VS for $p < 0.01$), and extremely significant (ES for $p < 0.001$). Each p -value table is followed by a second table, which contains the mean values of overlap, accuracy, sensitivity, and specificity for each group. Sections II and III are identical regarding the experiments, however, the pathologies of the masses

are different (Sec. II—malignant masses, Sec. III—benign masses). Although the experiments are identical they have been separated for clarity purposes.

A larger set of segmentation results has been placed in an image gallery containing 7 malignant mass results (Fig. 7) and 7 benign mass results (Fig. 8). These figures are located in the Appendix.

1. Segmentation results

2. ANOVA test results for comparison of contour groups with single observer: Malignant cases

TABLE II. Single observer results (expert A gold standard, malignant masses).

ANOVA test	P -value (group 1 vs group 2)	P -value (group 2 vs group 3)	P -value (group 1 vs group 3)
Difference between groups (overlap)	1.78×10^{-4} (ES)	2.91×10^{-2} (S)	NS
Difference between groups (accuracy)	NS	3.14×10^{-2} (S)	NS
Difference between groups (sensitivity)	1.88×10^{-9} (ES)	NS	1.85×10^{-13} (ES)
Difference between groups (specificity)	5.12×10^{-4} (ES)	2.40×10^{-3} (VS)	2.71×10^{-9} (ES)

TABLE III. Mean values for overlap, accuracy, sensitivity, and specificity (expert A gold standard, malignant masses).

Measurement	Mean value (group 1)	Mean value (group 2)	Mean value (group 3)
Overlap	0.47	0.60	0.53
Accuracy	0.88	0.90	0.87
Sensitivity	0.49	0.75	0.81
Specificity	0.99	0.94	0.88

TABLE IV. Single observer results (expert B gold standard, malignant masses).

ANOVA test	P -value (group 1 vs group 2)	P -value (group 2 vs group 3)	P -value (group 1 vs group 3)
Difference between groups (overlap)	3.96×10^{-6} (ES)	NS	1.58×10^{-4}
Difference between groups (accuracy)	NS	NS	NS
Difference between groups (sensitivity)	4.88×10^{-8} (ES)	4.31×10^{-2} (S)	4.25×10^{-12} (ES)
Difference between groups (specificity)	2.70×10^{-4} (ES)	4.36×10^{-4} (ES)	1.44×10^{-7} (ES)

TABLE V. Mean values for overlap, accuracy, sensitivity, and specificity (expert B gold standard, malignant masses).

Measurement	Mean value (group 1)	Mean value (group 2)	Mean value (group 3)
Overlap	0.38	0.54	0.51
Accuracy	0.83	0.86	0.84
Sensitivity	0.38	0.56	0.60
Specificity	1.00	0.98	0.94

3. ANOVA test results for comparison of contour groups with single observer: Benign cases

TABLE VI. Single observer results (expert A gold standard, benign masses).

ANOVA test	<i>P</i> -value (group 1 vs group 2)	<i>P</i> -value (group 2 vs group 3)	<i>P</i> -value (group 1 vs group 3)
Difference between groups (overlap)	3.19×10^{-4} (ES)	8.38×10^{-4} (ES)	NS
Difference between groups (accuracy)	NS	4.73×10^{-3} (VS)	2.51×10^{-3} (VS)
Difference between groups (sensitivity)	1.14×10^{-9} (ES)	1.89×10^{-2} (S)	7.51×10^{-17} (ES)
Difference between groups (specificity)	8.93×10^{-3} (VS)	1.24×10^{-3} (VS)	3.32×10^{-10} (ES)

TABLE VII. Mean values for overlap, accuracy, sensitivity, and specificity (expert A gold standard, benign masses).

Measurement	Mean value (group 1)	Mean value (group 2)	Mean value (group 3)
Overlap	0.46	0.58	0.45
Accuracy	0.90	0.91	0.85
Sensitivity	0.49	0.73	0.82
Specificity	0.99	0.94	0.86

TABLE VIII. Single observer results (expert B gold standard, benign masses).

ANOVA test	<i>P</i> -value (group 1 vs group 2)	<i>P</i> -value (group 2 vs group 3)	<i>P</i> -value (group 1 vs group 3)
Difference between groups (overlap)	8.82×10^{-5} (ES)	NS	1.62×10^{-2} (S)
Difference between groups (accuracy)	NS	2.62×10^{-2} (S)	2.48×10^{-2} (S)
Difference between groups (sensitivity)	1.61×10^{-7} (ES)	NS	3.14×10^{-12} (ES)
Difference between groups (specificity)	1.18×10^{-2} (S)	1.27×10^{-2} (S)	1.25×10^{-7} (ES)

TABLE IX. Mean values for overlap, accuracy, sensitivity, and specificity (expert B gold standard, benign masses).

Measurement	Mean value (group 1)	Mean value (group 2)	Mean value (group 3)
Overlap	0.36	0.51	0.44
Accuracy	0.88	0.89	0.83
Sensitivity	0.36	0.61	0.69
Specificity	0.99	0.94	0.86

4. ANOVA test results for comparison of contour groups between two observers

TABLE X. Two observer results: expert A vs expert B, malignant masses.

ANOVA test	<i>P</i> -value (group 1 vs group 2)	<i>P</i> -value (group 2 vs group 3)	<i>P</i> -value (group 1 vs group 3)
Expert A vs expert B (overlap)	3.12×10^{-3} (VS)	3.32×10^{-2} (S)	NS
Expert A vs expert B (accuracy)	1.20×10^{-2} (S)	4.46×10^{-2} (S)	NS
Expert A vs expert B (sensitivity)	9.43×10^{-4} (ES)	3.38×10^{-4} (ES)	3.67×10^{-4} (ES)
Expert A vs expert B (specificity)	NS	NS	NS

TABLE XI. Mean values for overlap, accuracy, sensitivity, and specificity (expert A vs expert B, malignant masses).

Measurement	Mean value, expert A (group 1)	Mean value, expert B (group 1)	Mean value, expert A (group 2)	Mean value, expert B (group 2)	Mean value, expert A (group 3)	Mean value, expert B (group 3)
Overlap	0.49	0.38	0.62	0.55	0.55	0.51
Accuracy	0.89	0.83	0.91	0.87	0.87	0.84
Sensitivity	0.52	0.38	0.75	0.60	0.82	0.68
Specificity	0.99	1.00	0.95	0.97	0.89	0.91

TABLE XII. Two observer results: expert A vs expert B, benign masses.

ANOVA test	<i>P</i> -value (group 1 vs group 2)	<i>P</i> -value (group 2 vs group 3)	<i>P</i> -value (group 1 vs group 3)
Expert A vs expert B (overlap)	NS	NS	NS
Expert A vs expert B (accuracy)	NS	NS	NS
Expert A vs expert B (sensitivity)	3.56×10^{-2} (S)	4.90×10^{-2} (S)	2.03×10^{-2} (S)
Expert A vs expert B (specificity)	NS	NS	NS

TABLE XIII. Mean values for overlap, accuracy, sensitivity, and specificity: expert A vs expert B, benign masses.

Measurement	Mean value, expert A (group 1)	Mean value, expert B (group 1)	Mean value, expert A (group 2)	Mean value, expert B (group 2)	Mean value, expert A (group 3)	Mean value, expert B (group 3)
Overlap	0.42	0.35	0.57	0.50	0.48	0.44
Accuracy	0.90	0.88	0.91	0.89	0.85	0.83
Sensitivity	0.44	0.36	0.71	0.61	0.79	0.69
Specificity	0.99	0.99	0.94	0.94	0.86	0.86

IV. DISCUSSION

A. Segmentation results

The ROI's shown in Figs. 3 and 4 demonstrate that the intensity produced by the maximum value is capable of accurately delineating the mass body contour, and in some cases this intensity corresponding to the maximum value produces a contour, which falls inside the mass body contour. This situation can be problematic because low segmentation sensitivities can produce large errors during the feature calculation and classification phases of CAD_x. Of the three available segmentation choices for each mass, it appears that the first steepest change location produces the contours with the strongest correlation in comparison to both gold standards. These contours appear to cover both the mass body contour as well as the extended borders. In some instances the region grows into some areas that are not declared as mass areas by the gold standards—we call this flooding—and fails to grow into other areas that have been declared as mass areas. Finally, the second steepest change location produces contours that also cover both the mass body contour as well as the extended borders, and, these contours tend to also include surrounding fibroglandular tissue; hence, the flooding phenomenon is a common occurrence. In the cases shown, it is clear that steepest change location 1 produces the best contours, in comparison to the gold standards, however, the ANOVA test results allow us to make such a claim. The following discussion is divided into five sections: single observer malignant results, single observer benign results, and two observer results (malignant and benign), algorithm performance, and an additional discussion on methods.

B. Malignant cases with single observer

For both the expert A and expert B gold standards, Tables II–V show a statistically significant difference between groups 1 and 2 on the basis of overlap and sensitivity, where the mean values of group 2 were higher than the mean values of group 1 for these statistics. These results are expected because as shown in the figures, the group 2 contours consistently covered more of the mass area (and correctly covered this mass area) as compared to the group 1 contours, according to both experts. There was a statistically significant difference in sensitivity between group 1 and group 3, where the mean of group 3 was higher than the mean of group 1. This difference is an expected result because out of all the groups, group 3 contours consistently covered the most mass area. For the expert B gold standard there was a statistically significant difference in overlap between group 1 and group 3, where the mean of group 3 was higher than the mean of group 1. This difference is also an expected result because, out of all the groups, the group 3 contours covered the most mass area correctly.

C. Benign cases with single observer

For the expert A traces there were statistically significant differences between the group 2 and group 3 traces on the

basis of overlap, accuracy, and sensitivity, where the group 2 mean values for overlap and accuracy were higher than those of group 3 (see Tables VI–IX). This difference is an expected result because it is likely that many of the group 3 contours contained flooded areas, which cause both of these values to be lower than those values of contours without flooded areas. The overlap and sensitivity values for group 2 were significantly higher than those of group 1. This difference is also an expected result because the group 2 contours not only covered more mass area but also covered this area correctly. Finally, the group 3 accuracy and sensitivity values were significantly higher than those for group 1. Again this difference is an expected result because the group 3 contours not only covered more mass area but they also covered this area correctly.

For the expert B gold standard there were statistically significant differences between the group 2 and group 3 traces on the basis of accuracy and sensitivity, where the group 2 mean values for overlap and accuracy were higher than those of group 3. This difference is an expected result because it is likely that many of the group 3 contours contained flooded areas, which cause both of these values to be lower than contours without flooded areas. There were statistically significant differences between group 1 and group 2 on the basis of overlap and sensitivity, where the mean values for group 2 were higher than the mean values for group 1. This is an expected result because the group 2 contours not only covered more mass area but they also covered this area correctly. There were statistically significant differences between group 3 and group 1 on the basis of overlap and sensitivity, where the mean values for group 3 were higher than those of group 1. Again this difference is an expected result because the group 3 contours not only covered more mass area but they covered this area correctly.

In nearly all cases for the single observer studies, it was expected that the specificity values for group 1 would always be higher than those for groups 2 and 3 because this contour always covered the smallest mass area; consequently its background was always highly correlated with the background areas dictated by the gold standards. Moreover, in some cases the group 2 and group 3 contours grew into areas that were not regarded as mass, but rather were regarded as background; therefore, their specificity values had a lower correlation with the gold standard as compared to the group 1 contours.

D. Malignant and benign cases with two observers

For the two observer studies, comparisons were made between experts A and B on a group-by-group basis in an effort to prove that there were significant differences between the two radiologists on the basis of overlap, accuracy, sensitivity, and specificity (see Tables X–XIII). For the malignant masses, there were statistically significant differences between the two experts on the basis of overlap, accuracy, and sensitivity. There was a statistically significant difference between the two experts for group 3 on the basis of sensitivity. For the benign masses, there were statistically significant differences between the two experts for all three groups on the

basis of sensitivity. For all cases, expert A's values were consistently higher than those of expert B. These statistically significant differences between the experts were expected due to their differences in opinion. The fact that expert A's mean values were higher than those for expert B, however, does not warrant the conclusion that expert A is a more reliable expert; however, it does warrant the conclusion that there is stronger agreement between the computer's results and expert A's traces. Furthermore, there were less statistically significant differences for the benign cases than for the malignant cases. This result is expected because, in general, benign masses have better defined borders, and thus the two experts were more likely to agree.

E. Algorithm performance

Apparently the chosen thresholds produce first steepest change location intensities that generate contours closely correlated with the expert traces. In some instances the second steepest change location is extremely far from the first steepest change location, which implies that the function in question increases very slowly; moreover, many of the second steepest change location intensities produce contours with flooded areas. For the majority of the cases in which the second steepest change location contour achieves a higher sensitivity value, but not a significantly higher sensitivity value, we can still choose the first steepest change location contour because the difference between the two contours is likely to be negligible.

In analyzing the probability-based cost functions, we found that those functions with very steep changes are typically associated with masses that have well-defined borders while those functions that increase slowly are associated with masses that have ill-defined borders. This phenomenon may make it necessary to develop an adaptive threshold process for the steepest change evaluation such that the functions are grouped into various categories (e.g., smooth versus steep), because a threshold value that is optimal for a steep function may not be optimal for a smooth function.

F. Additional discussion on methods used

In this study the steepest descent method appears to have the advantage of locating ill-defined margins as well as extensions such as malignant spiculations and projections for mammographic masses. If solely the human eye is used, it can be difficult to separate the mass from the surrounding fibroglandular tissue. Therefore, this method has the potential to complement the process of reading mammographic films. One of the downfalls of the method is its dependence upon the assumption that masses are generally light in color. This assumption impedes the region growing process because masses that contain darker areas and are surrounded on one or more sides by bright tissue can cause contours to flood into areas that are not actual mass tissue. Typically, this situation occurs for the mass located on the border of the breast region on a mammogram.

All of the segmentation methods surveyed in the introduction of this paper are excellent solutions for the problems

their authors set out to solve, however, in some cases it is difficult to make comparisons between different methods without the availability of a set of several visual results. In some studies, the focus was either to detect masses or to distinguish malignant from benign masses. Thus, the validation process did not take the form of a comparison with expert radiologist manual traces; but rather, features were calculated on the potential mass candidates and they were later classified as being mass tissue or normal tissue.¹⁰⁻¹³ The purpose of Li's study¹⁴ was to distinguish between normal and abnormal tissue; thus the authors did not provide any statistics such as overlap or accuracy. Nevertheless, the study contains a figure of 60 masses that contain both computer and radiologist annotations to give the reader an idea of the computer algorithm's performance. Te Brake and Karssemeijer's study⁹ used the overlap statistic to test the efficacy of their method. They indicated that the central mass area was delineated by the radiologist and their computer results were compared to these annotations. The Kupinski and Giger study¹⁶ also used the overlap statistic to test the efficacy of their method and set a threshold for which the mass was considered to be successfully segmented. For example, masses whose overlap values are greater than 0.7 imply that there was successful segmentation.

The technical method presented herein shows that the results obtained from the maximization of the composed probability density function (i.e., the cost function) are equivalent to those obtained from previous methods presented by previous investigators. However, the steepest change of the composed probability density function is the closest to radiologists' determinations.

V. CONCLUSION

We have shown that our fully automatic boundary detection method for malignant and benign masses can effectively delineate these masses using intensities, that correspond to the first steepest change location within their cost functions. Additionally, the method appears to be more highly correlated with one set of expert traces than with a second set of expert traces, regarding the accuracy and overlap statistics. This result shows that inter-observer variability can be an important factor in segmentation algorithm design, and it has motivated us to seek the opinions of more expert radiologists to test the robustness of our algorithm. The second steepest change location intensity will always yield contours with higher sensitivity values, however, it behooves us to choose the first steepest change location intensity because it avoids the risk of choosing contours that contain substantial flooding. In future work, a worthwhile study would run the experiments for different threshold values in an effort to discover the possibility of deriving an optimal threshold procedure. We believe that such a procedure would improve the method of choosing optimal contours.

ACKNOWLEDGMENTS

This work was supported by U.S. Army Grant Nos. DAMD17-03-1-0314, DAMD17-01-1-0267, and DAMD

17-00-1-0291, and NIH Grant No. RCM/NCRR/NIH 2G12RR00348. The authors would also like to thank the referees for their constructive comments and recommendations.

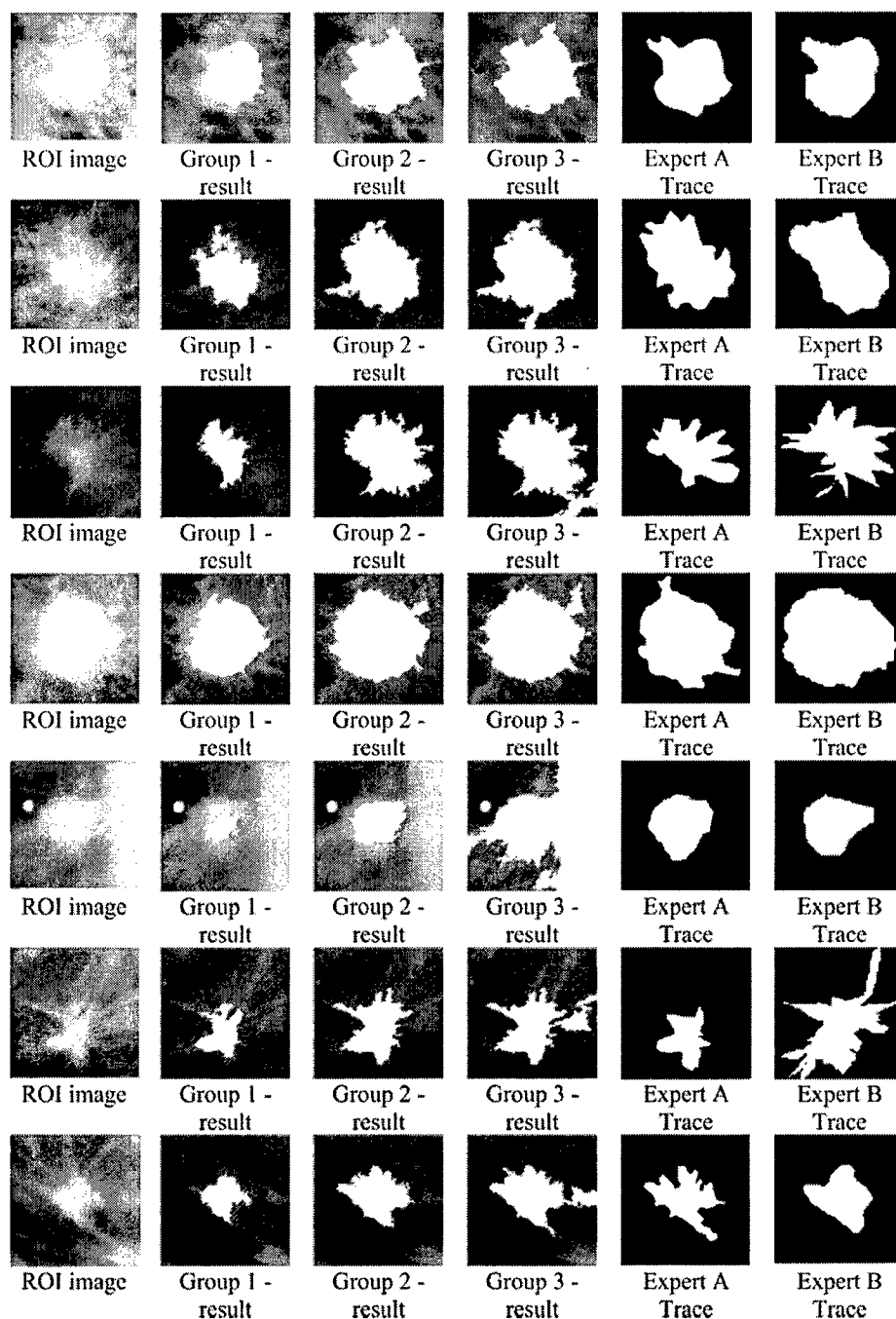
APPENDIX A—GALLERY OF SEGMENTATION RESULTS

FIG. 7. Segmentation results for a set of malignant masses.

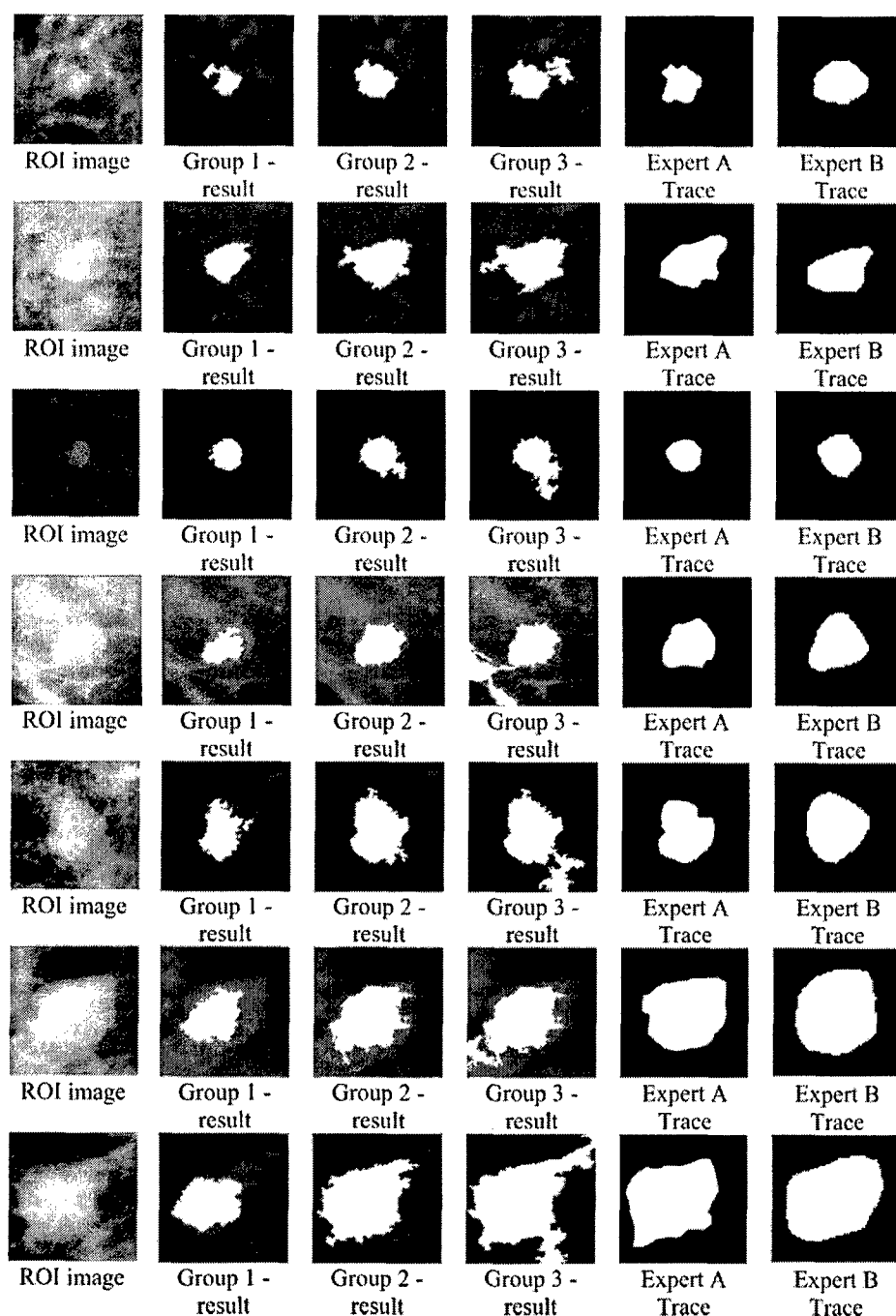


FIG. 8. Segmentation results for a set of benign masses.

^{a)} Author to whom correspondence should be addressed. Dr. Shih-Chung B. Lo, ISIS Center, Department of Radiology, Georgetown University, Box 571479, Washington, DC 20057-1479. Electronic mail: lo@isis.imac.georgetown.edu

¹ J. V. Lacey, Jr., S. S. Devesa, and L. A. Brinton, "Recent trends in breast cancer incidence and mortality," *Environ. Mol. Mutagen.* **39**, 82-88 (2002).

² J. E. Meyer, D. B. Kopans, P. C. Stomper, and K. K. Lindfors, "Occult breast abnormalities: percutaneous preoperative needle localization," *Radiology* **150**, 335-337 (1984).

³ A. L. Rosenberg, G. F. Schwartz, S. A. Feig, and A. S. Patchefsky, "Clinically occult breast lesions: localization and significance," *Radiology* **162**, 167-170 (1987).

⁴ B. C. Yankaskas, M. H. Knelson, M. L. Abernethy, J. T. Cuttino, and R.

L. Clark, "Needle localization biopsy of occult lesions of the breast," *Radiology* **23**, 729-733 (1988).

⁵ J. A. Harvey, L. L. Fajardo, and C. A. Innis, "Previous mammograms in patients with impalpable breast carcinoma: retrospective vs. blinded interpretation," *Am. J. Roentgenol., Radium Ther. Nucl. Med.* **161**, 1167-1172 (1993).

⁶ J. E. Martin, M. Moskowitz, and J. R. Milbrath, "Breast cancer missed by mammography," *Am. J. Roentgenol., Radium Ther. Nucl. Med.* **132**, 737-739 (1979).

⁷ J. R. Harris, M. E. Lippman, M. Morrow, and S. Hellman, *Diseases of the Breast* (Lippincott-Raven Publishers, Philadelphia, 1996), pp. 80-81.

⁸ J. E. Martin, *Atlas of Mammography: Histologic and Mammographic Correlations*, 2nd ed. (Williams and Wilkins, Baltimore, 1988), p. 87.

⁹ G. M. te Brake and N. Karssemeijer, "Segmentation of suspicious den-

- sities in digital mammograms." *Med. Phys.* **28**, 259–266 (2001).
- ¹⁰ L. Li, Y. Zheng, L. Zhang, and R. Clark, "False-positive reduction in CAD mass detection using a competitive classification strategy." *Med. Phys.* **28**, 250–258 (2001).
 - ¹¹ N. Petrick, H.-P. Chan, B. Sahiner, and D. Wei, "An adaptive density-weighted contrast enhancement filter for mammographic breast mass detection." *IEEE Trans. Med. Imaging* **15**, 59–67 (1996).
 - ¹² S. Pohlman, K. A. Powell, N. A. Obuchowski, W. A. Chilcote, and S. Grundfest-Broniatowski, "Quantitative classification of breast tumors in digitized mammograms." *Med. Phys.* **23**, 1337–1345 (1996).
 - ¹³ A. J. Méndez, P. G. Tahoces, M. J. Lado, M. Souto, and J. J. Vidal, "Computer-aided diagnosis: Automatic detection of malignant masses in digitized mammograms." *Med. Phys.* **25**, 957–964 (1998).
 - ¹⁴ H. Li, Y. Wang, K. J. R. Liu, S.-C. B. Lo, and M. T. Freedman, "Computerized radiographic mass detection—part I: lesion site selection by morphological enhancement and contextual segmentation." *IEEE Trans. Med. Imaging* **20**, 289–301 (2001).
 - ¹⁵ M. L. Comer, S. Liu, and E. J. Delp, "Statistical segmentation of mammograms." *Digital Mammography '96: proceedings of the 3rd international workshop on digital mammography*, Chicago, IL, pp. 475–478, 9–12 June 1996.
 - ¹⁶ M. A. Kupinski and M. L. Giger, "Automated seeded lesion segmentation on digital mammograms." *IEEE Trans. Med. Imaging* **17**, 510–517 (1998).
 - ¹⁷ S.-C. B. Lo, H. Li, Y. Wang, L. Kinnard, and M. T. Freedman, "A multiple circular path convolution neural network system for detection of mammographic masses." *IEEE Trans. Med. Imaging* **21**, 150–158 (2002).
 - ¹⁸ W. E. Polakowski, D. A. Cournoyer, S. K. Rogers, M. P. DeSimio, D. W. Ruck, J. W. Hoffmeister, and R. A. Raines, "Computer-aided breast cancer detection and diagnosis of masses using difference of Gaussians and derivative-based feature saliency." *IEEE Trans. Med. Imaging* **16**, 811–819 (1997).
 - ¹⁹ B. Sahiner, H.-P. Chan, N. Petrick, M. A. Helvie, and L. M. Hadjiiski, "Improvement of mammographic mass characterization using spiculation measures and morphological features." *Med. Phys.* **28**, 1455–1465 (2001).
 - ²⁰ R. M. Rangayyan, N. M. El-Faramawy, J. E. Leo Desautels, and O. A. Alim, "Measures of acutance and shape for classification of breast tumors." *IEEE Trans. Med. Imaging* **16**, 799–810 (1997).
 - ²¹ B. Sahiner, H.-P. Chan, D. Wei, N. Petrick, M. A. Helvie, D. D. Adler, and M. M. Goodsit, "Image feature selection by a genetic algorithm: Application to classification of mass and normal breast tissue." *Med. Phys.* **23**, 1671–1684 (1996).
 - ²² J. Suckling, D. R. Dance, E. Moskowicz, D. J. Lewis, and S. G. Blacker, "Segmentation of mammograms using multiple linked self-organizing neural networks." *Med. Phys.* **22**, 145–152 (1995).
 - ²³ B. Van Ginneken, "Automatic segmentation of lung fields in chest radiographs." *Med. Phys.* **27**, 2445–2455 (2000).
 - ²⁴ D. Downing and J. Clark, *Statistics the Easy Way*, 2nd ed. (Barron's Educational Series, Hauppauge, 1989), pp. 184–206.
 - ²⁵ W. Hopkins, *A New View of Statistics: P Values and Statistical Significance*; available online at www.sportsci.org/resource/stats/pvalues.html.
 - ²⁶ M. Heath *et al.*, "Current status of the digital database for screening mammography." *Digital Mammography* (Kluwer Academic, New York, 1998), pp. 457–460.

A Tumor-Targeted Nanodelivery System to Improve Early MRI Detection of Cancer

Kathleen Pirollo¹, John Dagata³, Paul Wang⁵, Matthew Freedman^{1,3}, A. Vladar⁴, Stanley Fricke²,
Lilia Ileva², Qi Zhou¹, and Esther H. Chang¹

¹ *Department of Oncology,* ² *Department of Neuroscience and* ³ *Department of Radiology,*
Georgetown University Medical Center, Washington, D.C.

⁴ *National Institute of Standards and Technology, Gaithersburg, M.D.*

⁵ *Department of Radiology, Howard University, Washington, D.C.*

*To whom correspondence should be addressed

Esther H. Chang, Ph.D.

Department of Oncology

Lombardi Comprehensive Cancer Center

Georgetown University Medical Center

3970 Reservoir Road, NW

The Research Building, TRB E420

Washington, D.C. 20057-1460

Tel: (202) 6878418

Fax: (202) 687-8434

Email: change@georgetown.edu

Running title: A Nanodelivery Complex for Early Cancer Detection

Keywords: Nanocomplex, tumor targeting, Magnevist®, MRI, Early detection

Abstract

The development of improvements in Magnetic Resonance Imaging (MRI) that would enhance sensitivity, dealing to earlier detection of cancer and visualization of metastatic disease is an area of intense exploration. We have devised a tumor targeting, liposomal nanodelivery platform for use in gene medicine. This systemically administered nanocomplex has been shown to specifically and efficiently deliver both genes and oligonucleotides to primary and metastatic tumor cells, resulting in significant tumor growth inhibition and even tumor regression. Here we examine the effect on MR imaging of incorporating conventional MRI contrast agent Magnevist® into our anti-transferrin receptor single chain antibody (TfRscFv) liposomal complex. Both *in vitro* and in an *in vivo* orthotopic mouse model of pancreatic cancer (CaPan-1), we show increased resolution and image intensity with the complexed Magnevist®. Using advanced microscopy techniques (SEM and SPM) we also established that the Magnevist® is in fact encapsulated by the liposome in the complex and that the complex still retains its nano-dimensional size. These results demonstrate that this TfRscFv-Liposome-Magnevist® nanocomplex has the potential to become a useful tool in early cancer detection.

Abbreviations:

Lip= liposome

Mag= Magnevist® (Gadopentetate Dimeglumine)

SEM= scanning electron microscopy

SPM= scanning probe microscopy

STEM= scanning transmission electron microscopy

TfRscFv= anti-transferrin receptor single chain antibody

TfRscFv-Lip-Mag= anti-transferrin receptor single chain antibody-liposome-Magnevist® complex

Introduction

The ability to detect cancer, both primary and metastatic disease, at an early stage would be a major step towards the goal of ending the pain and suffering from the disease. The development of tumor targeted delivery systems for gene therapy has opened the potential for delivery of imaging agents more effectively than is currently achievable. Magnetic resonance imaging (MRI) can acquire 3-Dimensional anatomical images of organs. Coupling these with paramagnetic images results in the accurate localization of tumors as well as longitudinal and quantitative: monitoring of tumor growth and angiogenesis. (1,2).

One of the most common paramagnetic imaging agents employed in cancer diagnostics is Magnevist® (Gadopentetate Dimeglumine). Gadolinium is a rare earth element. It shows paramagnetic properties since its ion (Gd^{++}) has seven unpaired electrons. The contrast enhancement observed in MRI scans is due to the strong effect of Gd^{++} primarily on the hydrogen-proton spin-lattice relaxation time (T_1). While free gadolinium is highly toxic, and thus unsuitable for clinical use, chelation with diethylenetriamine pentacetic acid (DTPA) generates a well tolerated, stable, strongly paramagnetic complex. This metal chelate is metabolically inert. However after i.v. injection of gadopentetate dimeglumine, the meglumine ion dissociates from the hydrophobic gadopentetate, which is distributed only in the extracellular water. It cannot cross an intact blood-brain barrier, and therefore does not accumulate in normal brain tissue, cysts, post-operative scars, etc, and is rapidly excreted in the urine. It has a mean half-life of about 1.6 hours. Approximately 80% of the dose is excreted in the urine within 6 hours.

A systemically administered tumor-targeting delivery system has been developed in our laboratory for use in gene medicine (3-8). This nano-sized complex is composed of a cationic liposome encapsulating the nucleic acid payload, which can be either genes (3-6) or oligonucleotides (7-8). Decorating the surface of the liposome is a targeting molecule which can be a ligand, such as folate or transferrin, or an antibody or an antibody fragment directed against a cell surface receptor. The presence of the ligand/antibody on the liposome facilitates the entry of the complex into the cells through binding of the targeting molecule by its receptor followed by internalization of the bound complex via receptor mediated endocytosis, a highly efficient internalization pathway (9,10.) This modification of the liposomes results in their being able not only to selectively deliver their payload to tumor cells, but also increases the transfection efficacy of the liposome. Transferrin receptor (TfR) levels are elevated in various types of cancer including oral, prostate, breast, and pancreas (11-16). Moreover, the TfR recycles during internalization in rapidly developing cells such as cancer cells (16), thus contributing to the uptake of these transferrin targeted nanocomplexes even in cancer cells where TfR levels are not elevated. The nanocomplex used in the studies described here employs an anti-transferrin receptor single chain anti-body fragment (TfRscFv) as the targeting moiety (17-18). TfRscFv contains the complete antibody binding site for the epitope of the TfR recognized by the monoclonal antibody 5E9 (18). TfRscFv has advantages over the Tf molecule itself, or an entire Mab, in targeting liposomes to cancer cells with elevated TfR levels: 1) the size of the scFv (28 kDa) is much smaller than the Tf molecule (80 kDa) or the parental Mab (155 kDa). The scFv-liposome-DNA complex may thus exhibit better penetration into small capillaries characteristic of solid tumors. 2) the smaller scFv has a practical advantage related to the scaled-up production necessary for the clinical trials. 3) the scFv is a recombinant molecule and not a blood product like Tf and thus presents no danger of a potential contamination by blood borne pathogens. 4)

without the Fc region of the Mab, the issue of non-antigen-specific binding through Fc receptors is eliminated (19). Most importantly, we have already shown that such an anti-TfR single chain antibody molecule can target an intravenously administered cationic liposome-DNA nanocomplex preferentially to tumors (5,6). Encapsulating Magnevist® within such a tumor-targeted nanocomplex offers potential advantages for enhanced sensitivity, detection of metastases and diagnosis of cancer.

In this manuscript we explore the use of this nanocomplex for systemic delivery of imaging agent Magnevist® to tumors using a mouse xenograft model of human pancreatic cancer. In addition, we employed Scanning Electron Microscopy (SEM) and Scanning Probe Microscopy (SPM) (20-25) to examine the physical structure and size of these Magnevist® carrying nanocomplexes. Since gadolinium is both a high-atomic number element and possess a large magnetic moment, these properties can be exploited in a variety of ways to enhance contrast in both SEM and SPM. The findings presented below demonstrate that our ligand liposome nanocomplex does indeed encapsulate Magnevist® and that intravenous administration of this complex results in enhanced tumor imaging.

Materials and Methods

Cell lines

Human lymphoblastic leukemia cell line K562 was obtained from the Lombardi Comprehensive Cancer Center Tissue Culture core facility. These suspension cells were maintained in RPMI1640 supplemented with 10% Heat Inactivated FBS plus 2mM L-Glutamine, and 50 ug/ml each of penicillin, streptomycin and neomycin. Human pancreatic cancer cell line CaPan-1 (obtained from ATCC Manassas, VA) was derived from a metastatic adenocarcinoma of the pancreas. It was maintained in Iscov's Modified Dulbecco's Medium containing 4mM L-Glutamine and Sodium Bicarbonate, supplemental with 20% non-Heat Inactivated FBS, 2mM L-Glutamine and 50 ug/mL each of penicillin, streptomycin and neomycin.

Nanocomplex Formation

Cationic liposome (DOTAP:DOPE) was prepared by the ethanol injection method as previously described (6). When delivering plasmid DNA, the full complex was formed in a manner identical to that previously described (26). To encapsulate the imaging agent, the TfRscFv was mixed with the liposome at a specific ratio (identical to that used with DNA) and incubated at room temperature for 10 minutes. Magnevist® was added to this solution, mixed and again incubated at room temperature for 10 minutes. For *in vitro* transfection 2 ml of serum-free media was added to the complex prior to transfection. When prepared for *in vivo* use, dextrose was added to a final concentration of 5%. For both *in vitro* and *in vivo* complex formation the ratio of Magnevist® to liposome was 1:7 (v:v).

In Vitro Transfection

To transfect suspension cells K562, 15×10^6 cells in a total volume of 4.0 ml of medium with all supplements except serum (serum free medium) were placed into a 100mm² tissue culture dish. Two ml of the transfection solution from above, containing varying amounts of Magnevist®, was added to the cell suspension. The plate was incubated at 37°C with gentle rocking for the length of time given in the Results section, after which the cells were gently pelleted (600xg for 7 minutes) at 4°C in 0.5ml microcentrifuge tubes and washed three times

with 10ml of serum free medium to remove any excess transfection solution and placed on wet ice until imaged.

In Vivo Tumor Targeting

To assess the tumor selective targeting of the TfrscFv-Lip nanocomplex to primary and metastatic tumors an orthotopic metastases model using human pancreatic cancer cell line CaPan-1 was used. Subcutaneous xenograft tumors of CaPan-1 were induced in female athymic nude mice by injection of 1×10^7 CaPan-1 cells suspended in Matrigel™ collagen basement membrane matrix (BD Biosciences). Approximately eight weeks later the tumors were harvested and a single cell suspension of the tumor was prepared. $1.2 - 1.5 \times 10^7$ cells, also suspended in Matrigel™ were injected into the surgically exposed pancreas of female athymic nude mice as previously described (27). Five weeks post-surgery, the complex carrying the LacZ gene was i.v. injected 3X over 24 hrs (at 40ug DNA/injection). 60 hrs later the animals were sacrificed and examined for the presence of metastases and organs stained for β -galactosidase expression using a previously described procedure (3).

MRI Imaging

For *in vitro* MRI imaging, the cell pellets in microcentrifuge tubes were positioned at the center of the magnet. The MR imaging was performed at Howard University using a 4.7T horizontal bore NMR machine (Varian Inc, Palo Alto, CA). The imaging protocols consist of a multi-slice T1-weighted spin echo imaging sequence and a saturation-recovery sequence. For the T1-weighted imaging technique, the repetition time (TR) was 1000ms, and the echo time (TE) was 13ms. The T1-weighted spin-echo imaging technique was applied to verify the positive image enhancement. The saturation-recovery MR sequence with variable echo times was used for the T1 measurement. The slice thickness of images was 0.5mm. The RF coil employed was a 30mm single loop coil. The RF coil serves as an RF transmitter and receiver. The RF pulse was a selective 5 ms sinc pulse. The number of phase encoding steps was 256. The field-of-view was 15 mm x 15 mm. The image area chosen in the study was located at the center of the RF coil for RF homogeneity. The MR images were taken in the cross-section direction of the microcentrifuge tube. The height of the cell pellet was 12mm. The range of the multi-slice images covers the whole pellet. The center slice images, which were not influenced by the image distortion due to the susceptibility effect from the air-pellet boundary, were utilized for the studies. The image intensity was measured using the Varian Image Browser software. The signal is taken from a region-of-interest, which is big enough to cover two thirds of the image from each microcentrifuge tube. The relative image intensities of the pellets from these tubes were applied for contrast enhancement evaluation and the T1 measurements.

For the *in vivo* studies, mice bearing CaPan-1 orthotopic tumors were employed. These studies were performed at Georgetown University. Animals to be imaged were anesthetized and placed in a proprietary, in-house designed, animal management system. This system incorporates a warm water heating system that maintains the temperature at 37°C, as well as a four channel thermal optical monitoring system used to monitor animal's skin temperature, ambient temperature and wall temperature of the device. For imaging, anesthesia was induced using isoflurane at 4%, with the remaining gas comprised of a 66% oxygen and 30% nitrous oxide mixture. Maintenance of anesthesia was achieved with 1.5% isoflurane under similar gaseous conditions of oxygen and nitrous oxide as noted. The anesthetized animal was positioned inside of a cylindrical variable radiofrequency resonant antenna (bird cage resonator

volume coil) and tuned to a center frequency of approximately 300 MHz (the resonant frequency of water molecules when subject to a field strength of 7 Tesla). The imaging protocol used was T1-weighted Turbo RARE (rapid acquisition with rapid enhancement) three-dimensional imaging sequences performed on a 7T Bruker Biopsin (Germany/USA) imaging console. The imaging parameters used were: T1-weighted Turbo-RARE 3D (3-dimensional), TE 13.3 ms, TR 229.5, Flipback on, 4 echoes with a field of view of 8.0/3.5/3.5 cm and a 256 x 256 x 256 matrix. After a baseline image was acquired, the animal was kept immobilized in the animal holder and the Magnevist® only (diluted to 400 ul with 1x Phosphate Buffered Saline pH=7.4) or the TfRscFv-Lip-Mag complex (total volume 400 ul) was systemically administered using a 27G needle by intravenous injection into the tail vein of the animal and the 3D imaging sequence was immediately initiated. The imaging with the two solutions were performed on sequential days.

Scanning Electron Microscopy

Sample solutions of liposome-encapsulated Magnevist contrast agent, and complete nanocomplex consisting of a tumor-targeting single-chain transferrin receptor protein coating the liposome-encapsulated complex, TfRscFv-Lip-Mag, were prepared at GUMC, delivered to NIST and were stored under dark and refrigeration until needed. For each imaging session, a fresh dilution 1:3 by volume with deionized water was prepared and a 5 uL droplet was micropipetted onto a standard 200-mesh TEM grid consisting of 30-60 nm formvar and 15-20 nm carbon. The droplet was allowed to dry on the grid in air for 5 minutes before loading into the vacuum chamber of the microscope. Imaging was performed using an Hitachi S-4800 field-emission microscope at NIST. Of particular interest to applications of SEM to NDA imaging is a comparison of upper and lower secondary electron detectors [SE9U) and SE(L)] – using the SEM in its usual mode – to the addition of a transmitted electron (TE) detector, transforming the instrument into a low voltage STEM.

Scanning Probe Microscopy

Samples solutions of liposome-encapsulated Magnevist contrast agent, and complete nanocomplex were prepared at GUMC, delivered to NIST and were stored under dark and refrigeration until needed. For each imaging session, a fresh dilution 1:3 by volume with deionized water was prepared and a 5ul droplet was micropipetted onto an ultrasonically cleaned silicon substrate used with native oxide or with a poly-L lysine coating. SPM imaging were obtained using a Veeco MultiMode microscope with a Nanoscope IV controller. Topography by tapping mode with Z control [Veeco RTESP cantilevers $f_0 \sim 320\text{-}360$ kHz and $k \sim 20\text{-}60$ N/m], phase imaging, and magnetic force microscopy using magnetic coated tips (Veeco MESP 68 kHz) were performed in life mode. Dynamic imaging of dewetting and surface energy “phase separation” as the solution evaporates to expose isolated nanoparticles and aggregates were used to understand the consequences of solvent drying on the stability of the particles and its effect on the various SPM contrast mechanisms available with the SPM system.

Results

Tumor Specific Targeting by the Ligand-Liposome Nanocomplex Carrying a Reporter Gene

To assess selective targeting of the TfRscFv-LipA nanocomplex to primary tumor and metastases an orthotopic metastasis model, a closer approximation of the clinical situation, using

human PanCa cell line CaPan-1 was employed. Surgical orthotopic implantations of CaPan-1 xenograft tumor sections into nude mice have been shown to produce within 56 days, metastases in liver and spleen (27). Orthotopic tumors of CaPan-1 were induced in female athymic nude mice as described in Methods. Approximately 5 weeks later, the animals were euthanized and necropsied to look for tumor in the pancreas and other organs. As shown in Figure 1A, extensive tumor growth is evident throughout the pancreas. Metastases were present in various organs in four of five mice including the spleen, liver, lung, adrenal gland and even within the diaphragm. This experiment was repeated with similar results.

To establish selective targeting tumor and metastasis, prior to sacrificing the mice, the TfRscFv-LipA complex carrying pSVb (LacZ) plasmid DNA for β -galactosidase expression was i.v. injected into the mice three times over a 24 hour period (40 μ g of plasmid DNA per injection). All five mice were sacrificed 60 hours post-injection and various organs including the liver, lung, spleen, pancreas and diaphragm were harvested and examined for the presence of metastasis and tumor specific staining. Fresh samples, sliced at 1 mm thickness, were stained with X-gal to produce a blue color where the gene is expressed. The tumor targeting ability and high transfection efficiency of the complex is demonstrated by the presence of the reporter gene in the various organs from this animal (Figure 1B). In the liver, lung, adrenal gland and diaphragm it is clearly shown that the reporter gene is highly expressed only in the metastases, while no blue color is evident in the adjacent normal tissue. The metastasis visible in the liver in Figure 1A (arrow) is the same tumor nodule strongly expressing β -galactosidase in Figure 1B (arrow) confirming the tumor specific nature of this nanocomplex. In some of the mice, growth of the tumor in pancreas also resulted in extrusion of tumor through the original incision site used for implantation. In Figure 1B this strongly blue stained subcutaneous tumor, surrounded by normal non-stained skin is also shown, again showing tumor cell specificity. Similar results were observed in the rest of the mice, and in the repeat experiment. Thus, this systemically administrated nanocomplex will target tumor cells both primary and metastatic, wherever they occur in the body, and efficiently deliver plasmid DNA. We wished to expand the potential of this delivery system to include contrast agents. The ability to do so could result in improved imaging and cancer detection.

In vitro Studies Using TfRscFv-Lip Complex to Deliver Magnevist®

As Magnevist® is one of the most frequently employed contrast agent in the clinic, it was chosen as for use in these studies. In our initial experiments we examined whether the complex could be prepared with Magnevist® and if doing so would enhance the MRI signal. Since trypsinization could lead to membrane damage and leakage of contrast agent from the cells, adherent cells were not employed in these studies. Instead, a human lymphoblastic leukemia cell line, K562, which grows as a suspension culture was used. Moreover, gentle pelleting and washing of the cells would remove any excess Magnevist® or complex prior to imaging, allowing only cell associated signal to be detected.

1. Time Dependent Image Enhancement by the TfRscFv-Lip-Mag Nanocomplex

We examined the optimal time for transfection of the TfRscFv-Lip-Magnevist nanocomplex. The suggested clinical dose of Magnevist is 0.1mMole/kg. In these initial studies we used a dose of 0.3mMole/kg (corrected for the smaller weight and blood volume of mouse versus man) in the complex per 250ul of transfection solution. K562 cells were transfected for times ranging from 20 to 90 minutes. Twenty minutes showed very low transfection activity

based upon the image intensity (data not shown). However, as shown in Figure 2A, by sixty minutes the cells transfected with the complex showed a large increase in intensity as compared to the untreated cells. The intensity of the untreated cells (202 ± 48) was not significantly different than that of an empty marker tube (194 ± 43) indicating that the cells themselves do not contribute to the signal detected. More importantly, the transfection efficiency plateaus at approximately 60 minutes since the relative intensity of the cells transfected for 60 and 90 minutes were identical (317 ± 46 and 317 ± 47 , respectively).

2. Magnevist® Dose Dependent Image Enhancement

Using 60 minutes as the transfection time we then assessed the effect of increasing amounts of Magnevist® on the TfRscFv-Lip-Mag complex image enhancement. The doses tested were 0.05, 0.3 and 0.9 mM/kg. Corrected for size and blood volume of the mouse, the volumes of Magnevist® used in the complex per 250ul of transfection solution were 0.25ul, 1.5ul and 4.5ul. As shown in Figure 2B and Table 1, the image intensity increases and the T1 relaxation time shortens as a function of the amount of contrast agent included in the complex.

3. Image Enhancement by TfRscFv-Lip-Mag as Compared to Free Magnevist®

Based upon the above experiments it appears that the TfRscFv-Liposome can complex with Magnevist® and deliver it to the cells for image enhancement. To assess the level of enhancement of the complexed contrast agent as compared to the agent alone and demonstrate that the signal obtained is not due to the presence of unincorporated Magnevist®, we treated K562 cells with either free Magnevist® or the TfRscFv-Lip-Mag nanocomplex. The identical amount of contrast agent (0.3uM/kg or 1.5ul/250ul transfection volume) and transfection time (60 minutes) was used for both solutions. While free Magnevist® showed enhanced contrast relative to the untreated cells as expected, the cells treated with the TfRscFv-Lip-Mag complex demonstrated a much greater increase in image intensity and shortened T1 relaxation time compared to both untreated and free Magnevist® treated cells (Fig. 2C, Table 2). These results not only demonstrate the increased efficiency of contrast agent uptake by means of the targeted nanocomplex, but also indicate that the observed signal is likely not due to uncomplexed Magnevist®. Further evidence of Magnevist® encapsulation is given below.

In Vivo Image Enhancement With TfRscFv-Lip-Mag

The above studies established that the nanocomplex could more efficiently image tumor cells *in vitro* than Magnevist® alone. However, to have potential for clinical use, the complex must exhibit a similar effect *in vivo*. We employed the same human pancreatic cancer orthotopic mouse model (CaPan-1) for these studies as was used above to demonstrate tumor specific targeting of the complex carrying a reporter gene. Mice bearing CaPan-1 tumors were imaged on a 7T Bruker NMR as described in Methods. Once positioned in the coil, a baseline image was obtained using a T1-weighted Turbo RARE (rapid acquisition with rapid enhancement) three-dimensional imaging sequence. To facilitate image alignment, after baseline acquisition the animal was maintained in the animal holder while the imaging solution was administered via intravenous injection. Signal acquisition was begun within three minutes of the injection. The amount of Magnevist® administered to the mouse, either free (as is performed in the clinic) or included in the complex was 10 ul. This amount is equivalent to 0.2mM/Kg or twice what is used in humans. This amount was selected since the standard human dose of 0.1 mM/Kg Magnevist® alone gave a very poor signal in the mice. The imaging with free Magnevist® and

the TfRscFv-Lip-Mag complex were performed on two consecutive days. A baseline scan was also performed prior to administration of nanocomplex to confirm that all of the Magnevist® from the previous day had been washed out. MR technique and windows were consistent between the two sets of images with the windows adjusted to correct for an automatic windowing feature of the scanner. Imaging of the Magnevist® and nanocomplex-Mag in two separate mice are shown in Figure 3. In Panel A, four months after surgical implantation of the CaPan-1 tumor cells, the animal is carrying a large orthotopic tumor. The increased resolution and signal intensity, as compared to the contrast agent alone is quite evident. Similar results are observed in the mouse shown in Panel B. This animal, only two months post-surgery, has a visible subcutaneous tumor growing through the site of the incision. A small abdominal mass was also detected by palpation. Not only is the signal in the subcutaneous tumor more enhanced after administration of the complexed Magnevist®, but what appears to be the small orthotopic tumor (arrow) is evident in this scan and not in the one in which the animal received the free Magnevist®. These studies thus establish that when Magnevist® is incorporated within the TfRscFv-Liposome complex there is an improved tumor visualization in an *in vivo* situation, and they suggest the potential benefit of further developing this means of tumor detection for clinical use.

Physical Characterization Studies

While the *in vitro* studies offered circumstantial evidence that complexed Magnevist® is encapsulated within the liposome, we have employed sophisticated microscopy techniques (SEM and SPM) to confirm this fact and further characterize (e.g. complex size) the TfRscFv-Lip-Mag complex.

1. Imaging of liposomes without Magnevist

High-resolution imaging implies narrow depth of focus and so requires relatively thin and flat samples. How thin varies with technique, but surface and substrate effects -- surface energy and symmetry lowering -- often dominate the structural forces typical of biomaterials. This is particularly true in the case of liposomes given their tenuous nature. (28) So an understanding of reliable methods for preparing and characterizing the dimensional and mechanical stability of isolated liposomes is an essential step. The goal of our present characterization efforts is perform direct sensing of the mechanical stiffness and magnetic properties of nanoparticles to establish that the contrast agent is indeed contained within the nanoparticle and not simply associated externally with the liposomes.

The SPM images surface topography in tapping mode by oscillating the tip and cantilever to which it is attached close to the cantilever resonance frequency. A feedback circuit maintains the oscillation of the cantilever at a constant amplitude. This constant amplitude is given by a set point which is somewhat smaller than that of the freely oscillating cantilever. Since the SPM tip interacts with the surface through various small forces, there is a phase shift between the cantilever excitation and its response at a given point on the surface. For an inhomogeneous surface, the tip-surface interactions will vary according to surface charge, steep topographical changes, and mechanical stiffness variations, for example. By changing the set point and observing how certain features respond to softer or harder tapping, we can correlate this with the response expected for a specific structure such as a liposome. (The free oscillation amplitude signal is approximately 1.78 V.) A sequence of SPM phase images of a pair of isolated liposomes without payload is shown in Figure 4. Figure 4A was imaged at a set point of 1.68 V

and the corresponding negative phase difference between the substrate and liposome indicates that the tip-sample interaction is attractive for the liposome, given by a phase value of -3.5 degrees. In the case of an attractive interaction and negative phase, the phase image of the liposome appears dark, except for a topographically keyed ring at the liposome edge. Figure 4B demonstrates the effect of reducing the set point to 1.45 V: The liposome now appears bright since the tip-sample interaction becomes repulsive, and in this case the phase difference between the liposome and substrate is $+8$ degrees. Finally, Figure 4C shows that the phase difference recorded at a set point of 1.35 V increases further, becoming $+35$ degrees.

2. Imaging of liposome-encapsulated Magnevist

Figure 5 presents SPM and SEM images of isolated liposome-encapsulated Magnevist (Lip+Mag) nanoparticles. The size distribution of single Lip+Mag particles is in the range of 100 - 200 nm diameter and scales according to optical measurements that indicate that payload-encapsulating liposomes are approximately 50% larger than liposomes alone in their spherical state.

The SPM topograph appearing in Figure 5A indicates that liposomes containing Magnevist have a bimodal surface shape after drying that is more complex than that of the simple elliptical surface of a liposome containing no payload (not shown). The SPM phase behavior differs markedly from that of payloadless liposomes, the outer ring is repulsive relative to the center, and a corresponding SPM phase image is shown in Figure 5B. Regions of both attractive and repulsive tip-sample interaction appear at moderate set point values. A correlation between the SPM phase image obtained at a set point of 1.6 and the SEM image in TE mode is evident in Figures 5B and 5C. Liposomes appear uniformly bright across the entire particle in SEM images (not shown), similar to the uniform phase images we obtain by SPM.

3. Imaging of TfRscFv-Lip-Mag Nanocomplex

The complete TfRscFv-Lip-Mag nanocomplex was prepared and imaged by SEM and SPM as described in Methods. Results, shown in Figure 6 indicate that the solvent film undergoes phase separation; however, examples of isolated NDS can be readily observed on the dried film. Note that the SEM beam clearly causes some damage to the film, but the particles can be repeatedly scanned several times before beam damage becomes significant. The appearance of the full complex is different from that of the (Lip+Mag) only. The shape is less regular, and considerable texturing of the liposome surface following drying is consistent with protein denaturation. Also, SEM TE images indicate that the well-defined boundary between the outer ring and center of the liposome seen with the (Lip+Mag) particles is less apparent and the shape much more variable. This is consistent with the view that the presence of protein within the liposome has altered the osmotic outflow across the liposome during film drying.

It is possible to obtain additional information about these NDS particles by using the magnetic force microscopy imaging capabilities of the SPM (MFM). Since the magnetic moment of gadolinium-containing Magnevist is quite large, it should be possible using a magnetized SPM tip to interact with the oriented Magnevist concentrated within the liposomes. This is shown in Figure 7 for MFM of several approximately 100 - 200 nm diameter nanocomplexes. We establish that in fact we are producing an image which is truly magnetic in nature by using the lift-mode capabilities of the SPM: In this mode, a topographic image under normal tapping mode conditions is obtained. The reference surface information is then used to offset the tip by a specified height away from the surface and the surface is then scanned at this increased height.

This removes the influence of topography on the signal. MFM images obtained in lift-mode at a height of 15 nm or more from the surface are given by the magnetic phase image. The appearance of a signal confirms the presence of gadolinium encapsulated within the complex.

Discussion

The development of nanoparticle sized delivery systems which have greater tumor and tissue penetrance is a major direction in medical research in general and cancer research in particular. Combining the capabilities of these small particles with the ability to home specifically to tumor cells wherever they occur in the body could lead to significant advances in cancer treatment and diagnosis. We have previously shown that our ligand-liposome-DNA complex can specifically target and efficiently transfect tumor cells (primary and metastatic) (3-8). When encapsulating plasmid DNA this targeted delivery system is truly a nanocomplex, with a uniform size of less than 100nm (29). Used in combination with conventional radiation/chemotherapy delivery of therapeutic genes such as wild-type p53 by means of this nanodelivery system has resulted in tumor growth inhibition and even tumor regression in animal models (3-5,29). This tumor regression, and concomitant decrease in blood flow due to p53 mediated anti-angiogenesis, has also been demonstrated using Power Doppler Ultrasound Imaging (30). Adapting such a tumor targeted nanocomplex to deliver imaging agents would have the potential to improve early diagnosis as well as detection of metastatic disease. The results described above demonstrate that we can encapsulate and deliver the commonly used MR imaging agent Magnevist®, to tumor cells both *in vitro* and in an orthotopic animal model and in doing so produce a more defined and intense image than seen with uncomplexed Magnevist®.

Other nanometer sized delivery systems for contrast agents are being developed. A chylomicron remnant-like vehicle of approximately 90nm containing polyiodinated triglyceride analogs in a neutral lipid core has been developed as a hepatocyte-selective contrast agent for CT in animals (31). A paramagnetic liquid perfluorocarbon nanoparticle of approximately 250nm to which an anti- α (V) β 3 antibody has been conjugated, is being developed for MR imaging to assess angiogenesis and atherosclerosis (32-33). However, none of these are tumor targeting or currently applicable for cancer. However, given, as shown in Figure 1, that our nanocomplex can target metastatic disease it is anticipated that use of the nanocomplexed-Magnevist® would also enhance detection sensitivity for metastases. The results shown here are with primary tumors. Studies are currently underway to compare the sensitivity of detection between free Magnevist® and the TfRscFv-Lip-Mag complex in metastases.

Using SEM and SPM we have also shown that the TfRscFv-liposome complex maintains its nanometer size when Magnevist® is encapsulated (particles of approximately 100-200 nm are shown in Figure 6 and 7). We have also demonstrated that the structural and mechanical properties of liposomes containing a payload are sufficiently different from those without one for it to be possible to confirm that Magnevist® is indeed encapsulated with the liposome. This was further confirmed by MFM imaging of the complex.

A tentative explanation for the internal structure of (Lip+Mag) is that the slight bulge in the SPM topographic image, represents a liposome-confined phase separation, i.e., formation of a dense Magnevist-lipid toroidal distribution around the periphery of the particle with an preferential aqueous phase at the particle's center. This response is probably attributable to several important factors: First, the properties of Magnevist solution are pH \sim 6.5-8, an osmolality of 1,960 and viscosity of 4.9 at 20 oC according to the manufacturer. A plausible

chemical basis for this separation of the solution noted in the Magnevist data sheet: The meglumine salts dissociate completely from the complex, so changes in the local osmotic conditions. Coupled with the charge interaction of the gadolinium complex and cationic lipid, these interactions may provide a strong driving force for a hypertonic phase separation within the liposome. The charge distribution between the cationic lipid and Magnevist solution is effective at stabilizing the liposome and providing structural support in solution, and apparently in the bloodstream. This enhanced structural support is an important benefit for our studies since it allows most particles to remain intact during the film drying process, in contrast to the extensive decomposition observed with the liposome only solutions.

Therefore, we have been able to successfully encapsulate an MR contrast agent in our tumor targeted nanodelivery system. The image enhancement demonstrated by the complex over conventionally delivered Magnevist® indicates the potential of this system to improve early detection of cancer via MRI.

Acknowledgements

We wish to thank Ms. Brianna Kalk, Ms. Angelique Forrester, and Mr. Luis Torres for assistance in preparation of this manuscript, as well as the LCCC Animal Research Resource and Tissue Culture Shared Resource Facilities for their assistance in these studies. This work was supported in part by grants from NCI (CA103579-01) and SynerGene Therapeutics Inc to K.F.P., from NFCR to E.H.C, and from DAMD17-00-1-0291 to PCW.

References

1. Gillies,R.J., Bhujwalla,Z.M., Evelhoch,J., Garwood,M., Neeman,M., Robinson,S.P., Sotak,C.H., and Van Der,S.B. (2000). Applications of magnetic resonance in model systems: tumor biology and physiology. *Neoplasia (New York)* **2**, 139-151.
2. Degani,H., Chetrit-Dadiani,M., Bogin,L., and Furman-Haran,E. (2003). Magnetic resonance imaging of tumor vasculature. *Thrombosis & Haemostasis* **89**, 25-33.
3. Xu L and Pirollo K, Tang W Rait A Chang EH. (1999). Transferrin-liposome-mediated systemic p53 gene therapy in combination with radiation results in regression of human head and neck cancer xenografts. *Human Gene Therapy* **10**, 2941-2952.
4. Xu, L., Pirollo, K., Chang, E. H., and Murray, A. (1999) Systemic p53 gene therapy in combination with radiation results in human tumor regression. *Tumor Targeting* **4**, 92-104.. Stockton Press.
5. Xu,L., Tang,W.H., Huang,C.C., Alexander,W., Xiang,L.M., Pirollo,K.F., Rait,A., and Chang,E.H. (2001). Systemic p53 gene therapy of cancer with immunolipoplexes targeted by anti-transferrin receptor scFv. *Molecular Medicine* **7**, 723-734.
6. Xu L, Huang C-C, Huang W-Q, Tang W-H, Rait A, Yin Y, Cruz I, Xiang L-M, Pirollo K, and Chang E.H. (2002). Systemic Tumor-targeted Gene Delivery by Anti-Transferrin Receptor scFv-Immunoliposomes. *Molecular Cancer Therapeutics* **1**, 337-346.
7. Rait, A., Pirollo, K.F., Xiang, L.M., Ulick, D. and Chang, E.H. (2002). Tumor-Targeting, Systemically Delivered Antisense HER-2 Chemosensitizes Human Breast Cancer Xenografts Irrespective of HER-2 Levels. *Molecular Medicine* **8**, 476-487 .

8. Rait, A., Pirollo, K.F., Ulick, D., Cullen, K., and Chang, E.H. (2003). HER-2-Targeted Antisense Oligonucleotides Result in Sensitization of Head and Neck Cancer Cells to Chemotherapeutic Agents. *Ann. N.Y. Acad. Sci.* **1002**, 1-12.
9. Cristiano, R.J. and Curiel, D.T. (1996). Strategies to accomplish gene delivery via the receptor-mediated endocytosis pathway. *Cancer Gene Therapy* **3**, 49-57.
10. Cheng, P.W. (1996). Receptor ligand-facilitated gene transfer: enhancement of liposome-mediated gene transfer and expression by transferrin. *Human Gene Therapy* **7**, 275-282.
11. Keer, H.N., Kozlowski, J.M., Tsai, Y.C., Lee, C., McEwan, R.N., and Grayhack, J.T. (1990). Elevated transferrin receptor content in human prostate cancer cell lines assessed in vitro and in vivo. *Journal of Urology* **143**, 381-385.
12. Rossi, M.C. and Zetter, B.R. (1992). Selective stimulation of prostatic carcinoma cell proliferation by transferrin. *Proceedings of the National Academy of Sciences of the United States of America* **89**, 6197-6201.
13. Elliott, R.L., Elliott, M.C., Wang, F., and Head, J.F. (1993). Breast carcinoma and the role of iron metabolism. a cytochemical, tissue culture, and ultrastructural study. *Ann. N.Y. Acad. Sci.* **698**, 159-166.
14. Thorstensen, K. and Romslo, I. (1993). The transferrin receptor: its diagnostic value and its potential as therapeutic target. *Scandinavian Journal of Clinical & Laboratory Investigation - Supplement* **215**, 113-120.
15. Miyamoto, T., Tanaka, N., Eishi, Y., and Amagasa, T. (1994). Transferrin receptor in oral tumors. *International Journal of Oral & Maxillofacial Surgery* **23**, 430-433.
16. Ponka, P. and Lok, C.N. (1999). The transferrin receptor: role in health and disease. *International Journal of Biochemistry & Cell Biology* **31**, 1111-1137.
17. Haynes, B.F., Hemler, M., Cotner, T., Mann, D.L., Eisenbarth, G.S., Strominger, J.L., and Fauci, A.S. (1981). Characterization of a monoclonal antibody (5E9) that defines a human cell surface antigen of cell activation. *Journal of Immunology* **127**, 347-351.
18. Batra, J.K., Fitzgerald, D.J., Chaudhary, V.K., and Pastan, I. (1991). Single-chain immunotoxins directed at the human transferrin receptor containing Pseudomonas exotoxin A or diphtheria toxin: anti-TFR(Fv)-PE40 and DT388-anti-TFR(Fv). *Molecular & Cellular Biology* **11**, 2200-2205.
19. Jain, R.K. and Baxter, L.T. (1988). Mechanisms of heterogenous distribution of monoclonal antibodies and other macro-molecules in tumors: significance of elevated interstitial pressure. *Cancer Research* **48**, 7022-7032.
20. Wolfert MA., Schacht EH., Toncheva V., Ulbrich K., Nazarova O., and Seymour LW. (1996). Characterization of vectors for gene therapy formed by self-assembly of DNA with synthetic block co-polymers. *Human Gene Therapy* **7**, 2123-33.
21. Dunlap DD., Maggi A., Soria MR., and Monaco L. (1997). Nanoscopic structure of DNA condensed for gene delivery. *Nucleic Acids Research* **25**, 3095-101.
22. Kawaura C., Noguchi A., Furuno T., and Nakanishi M. (1998). Atomic force microscopy for studying gene transfection mediated by cationic liposomes with a cationic cholesterol derivative. *FEBS Letters* **421**, 69-72.
23. Choi YH., Liu F., Choi JS., Kim SW., and Park JS. (1999). Characterization of a targeted gene carrier, lactose-polyethylene glycol-grafted poly-L-lysine and its complex with plasmid DNA. *Human Gene Therapy* **10**, 2657-65.

24. Diebel CE., Proksch R., Green CR., Neilson P., and Walker MM. (2000) Magnetite defines a vertebrate magnetoreceptor. *Nature* **406**, 299-302.
25. Rasa, M., Kuipers, B.W.M., and Philipse, A.P. (2002). Atomic Force Microscopy and Magnetic Force Microscopy Study of Model Colloids. *J. Coll. Interface Sci* **250**, 303-315.
26. Wei Yu, Kathleen F. Pirollo, Bin Yu, Antonina Rait, Laiman Xiang, Weiqun Huang, Qi Zhou, Gozen Ertem, and Esther H. Chang. (2004) Enhanced transfection efficiency of a systemically delivered tumor-targeting immunolipoplex by inclusion of a pH-sensitive histidylated oligolysine peptide. *Nucleic Acids Research*, **5**.
27. Alisauskas, R., Wong, G.Y., and Gold, D.V. (1995). Initial studies of monoclonal antibody PAM4 targeting to xenografted orthotopic pancreatic cancer. *Cancer Research* **55**, 5743s-5748s.
28. Foo, J. J., Chan, V., and Liu, K.K. (2003) Contact Deformation of Liposome in the Presence of Osmosis. *Annals of Biomedical Engineering* **31**, 1279-1286.
29. Xu L, Frederick P, Pirollo K, Tang W, Rait A, Xiang L, Huang W-Q, and Chang EH (2002). Self-assembly of a virus-mimicking nanostructure system for efficient tumor-targeted gene delivery. *Human Gene Therapy* **13**, 469-481.
30. Freedman, M., Sarcone, A., Pirollo K.F., Lin, C., and Chang E.H. (2001). Ultrasound images of implanted tumors in nude mice using Sono-CT® correlated with MRI appearance. *SPIE Medical Imaging: Physiology and Function from Multidimensional Images* **4321**, 163-167.
31. Wisner, E.R., Weichert, J.P., Longino, M.A., Counsell, R.E., and Weisbrode, S.E. (2002). A surface-modified chylomicron remnant-like emulsion for percutaneous computed tomography lymphography: synthesis and preliminary imaging findings. *Investigative Radiology* **37**, 232-239.
32. Winter, P.M., Morawski, A.M., Caruthers, S.D., Fuhrhop, R.W., Zhang, H., Williams, T.A., Allen, J.S., Lacy, E.K., Robertson, J.D., Lanza, G.M., and Wickline, S.A. (2003). Molecular imaging of angiogenesis in early-stage atherosclerosis with alpha(v)beta3-integrin-targeted nanoparticles. *Circulation* **108**, 2270-2274.
33. Morawski, A.M., Winter, P.M., Crowder, K.C., Caruthers, S.D., Fuhrhop, R.W., Scott, M.J., Robertson, J.D., Abendschein, D.R., Lanza, G.M., and Wickline, S.A. (2004). Targeted nanoparticles for quantitative imaging of sparse molecular epitopes with MRI. *Magnetic Resonance in Medicine* **51**, 480-486.

Figure Legends

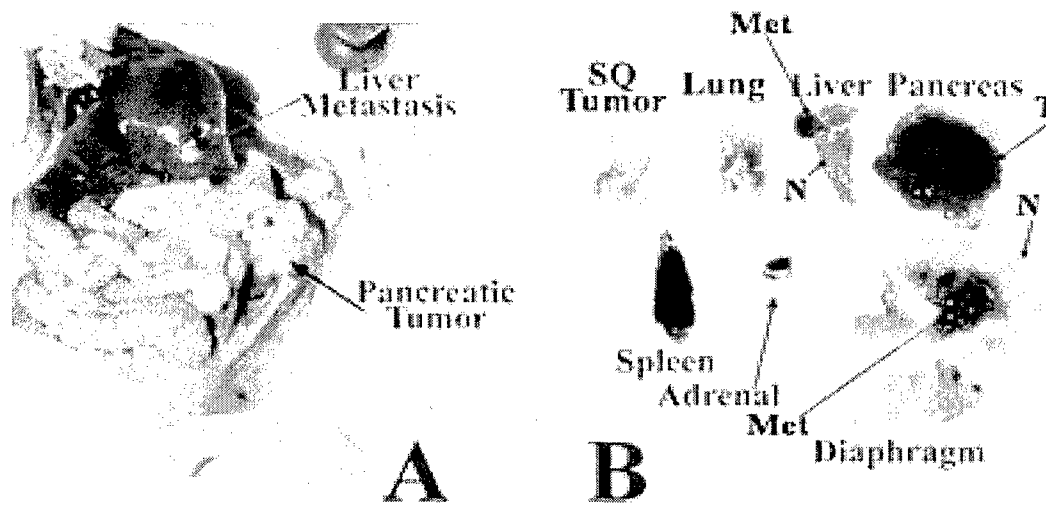


Figure 1: Tumor-specific targeting of a CaPan-1 orthotopic metastasis model by the TfRscFv-Liposome-DNA nanocomplex

Subcutaneous CaPan-1 xenograft tumors were induced in female athymic nude mice as described in Methods. The tumors were harvested and a single cell suspension in MATRIGEL® was injected into the surgically exposed pancreas. 5 wks post injection the TfRscFv-Liposome complex carrying the LacZ gene for β -galactosidase expression (40ug) was i.v. injected 3X over 24 hours. 60 hrs later the animals were sacrificed and examined for the presence of metastases and the organs stained for β -galactosidase expression. The same tumor nodule in the liver indicated by an arrow in **A** exhibits intense β -galactosidase expression in **B**. **A**= gross necropsy; **B**= tissues after staining for β -galactosidase.

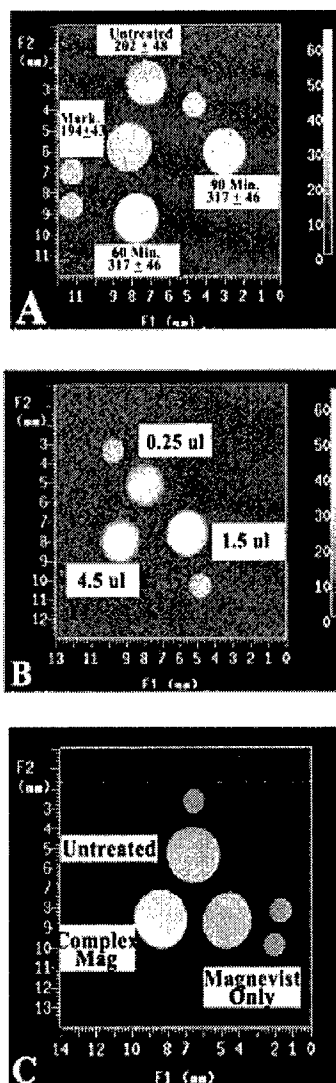


Figure 2: *In Vitro* MR Imaging of K564 cells after transfection with the TfrRscFv-Lip-Mag nanocomplex. After transfection with either free Magnevist® or the noncomplex encapsulating Magnevist® the cells were pelleted, washed with serum free medium and MR imaging performed using a 4.7T Varian NMR. The imaging protocol consisted of T1 weighted spin echo imaging sequences (TR/TE, 1000ms/13ms) to verify the image enhancement and a saturation-recovery MR sequence with variable echo times for the T1 measurement. Panel A = time dependent transfection. The values given are relative intensity. Panel B = shows variation in relative intensity with the amount of Magnevist® included in the complex (in ul). Panel C = Comparison of relative intensity of the TfrRscFv-Lip-Mag complex versus free Magnevist®. The small circles in all images are markers for sample orientation.

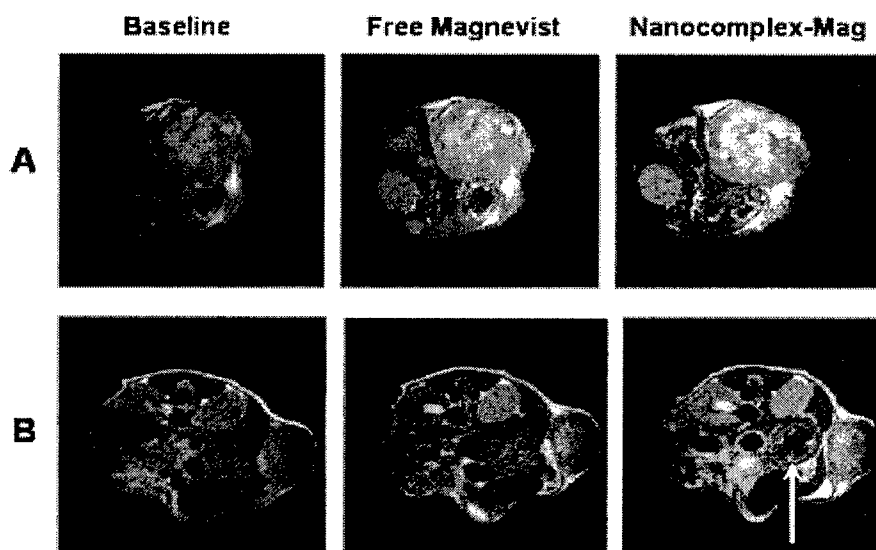


Figure 3: Improved MR imaging in a mouse model of pancreatic cancer using the Ligand-Liposome-Mag nanocomplex.

Human pancreatic cancer cell line (CaPan-1) cells were surgically implanted into the body of the pancreas of female athymic nude mice. Free Magnevist® (10ul) or the TfRscFv-liposome nanocomplex containing 10 ul of Magnevist® was i.v. injected (via the tail vein) into the mice on two consecutive days. This amount of Magnevist® is equivalent to twice the dose that would be administered to a human patient. The total volume of solution administered in both cases was 400ul. A baseline scan was performed just prior to administration of the nanocomplex to confirm that all of the Magnevist® from the previous day had been washed out. MR technique and windows were constant between the two sets of images with the windows adjusted to correct for an automatic windowing feature of the scanner. Panel **A** shows the differences in MRI signal in a large orthotopic tumor (4 months after surgical implantation of the tumor) between the i.v. administered free contrast agent and the TfRscFv-Lip-Mag complex. Panel **B** shows a similar effect in a second mouse with a subcutaneous tumor and a much smaller abdominal tumor (indicated by the arrow).

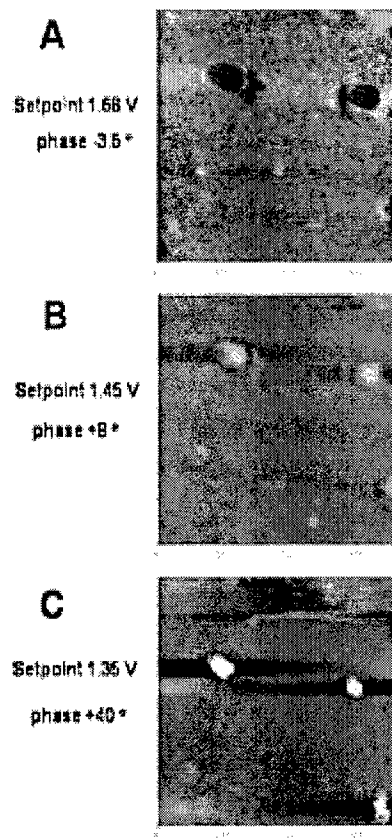


Figure 4: SPM phase images of liposomes without Magnevist®.

The images appearing in **A**, **B** and **C** were obtained at setpoints of 1.68 V, 1.45 V, and 1.35 V, respectively. The corresponding phase differences between the noncompliant substrate and the mechanically compliant liposome are -3.5° , $+8^{\circ}$, and $+40^{\circ}$. The interaction of the SPM tip and liposome changes from attractive to repulsive as the setpoint is decreased.

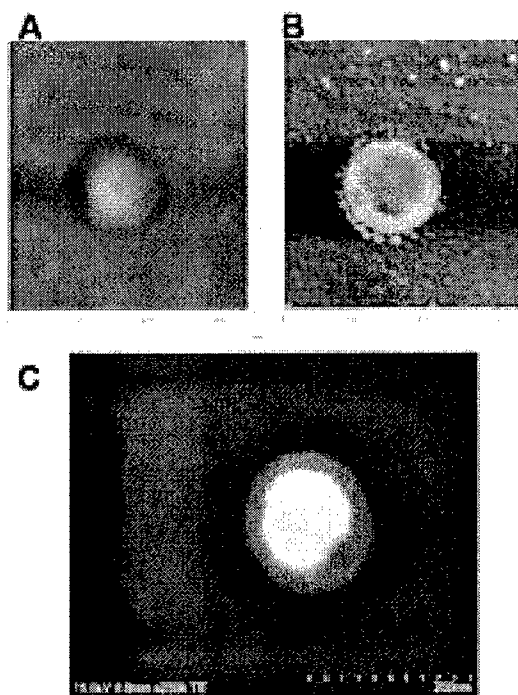


Figure 5: SPM and SEM images of liposome-encapsulated Magnevist® (Lip+Mag). **A** is the Atomic Force Microscopy topographical image of the Liposome encapsulated Magnevist® particle. The SPM phase image (setpoint = 1.6) (**B**) and 15 keV SEM (TE) [Transmission-mode electron detector] image (**C**) possess similar contrast, although generated by entirely distinct complementary physical mechanisms.

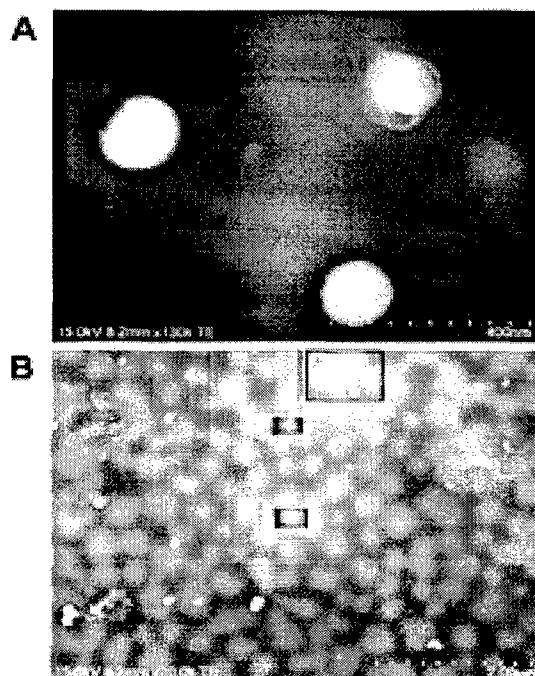


Figure 6: SPM topographic and phase imaging of TfRscFv+Lip+Mag nanocomplex. **A** is the 15 keV SEM (TE) [Transmission-mode electron detector] image of the full nanocomplex. A suitable choice of amplitude setpoint readily distinguishes intact nanocomplex particles from decomposition products. It is not known if the decomposed material was present in the solution prior to sample preparation or is the direct result of interaction with the substrate. **B**= A lower power image of the field. The boxed area is the image in **A**.

- 1) *Brain*
- 2) *Experimental Neurology*

MRI and Histological Correlations Of Cortical Brain Volumes In APP/PS1 Mice

Manaye, KF¹, Wang, P¹, O'Neil, J¹, Oei, A¹, Huaifu, S¹, Tizabi, Y¹, Ingram, DK², Mouton, PR^{2,3}

¹Howard University School of Medicine, Washington, D.C., ²Laboratory of Experimental Gerontology, National Institute on Aging, NIH, Baltimore, MD, ³Stereology Resource Center, Chester, MD.

Running title: Neuroimaging in APP/PS1 mice

Total words 2145 (abstract 285), 1 Table, 4 Figures, 9 pages, 27 References.

Address correspondence to:

Kebreten F. Manaye, M.D.
Department of Physiology and Biophysics
Suite 2305, Adams Bldg.
Howard University College of Medicine
520 W. Street, N.W.
Washington, DC 20059
Ph: 202.806.6337
Fax: 202-806-4479
Email: kmanaye@howard.edu

Abstract

Quantitative analyses indicate that brain atrophy on ante-mortem neuroimages and post-mortem tissue strongly correlates with the severity of cognitive impairment in Alzheimer's disease (AD). The absence of cortical atrophy in the age-matched, non-demented elderly suggests that volumetric studies of ante-mortem neuroimages may provide an early marker of AD in aging populations. In this study we used design-based stereology to quantify cortical volumes in double transgenic mice that deposit AD-type mutant β -amyloid proteins ($A\beta$) in cortical tissue. Spin-echo T1-weighted, high-resolution magnetic resonance imaging (MRI) was applied to the brains of male and female double transgenic mice aged 4-28 months of age that co-express AD-type mutations in amyloid precursor protein (APP) and presenilin-1 (PS-1), and, age-matched non-tg littermate controls (wild-type, WT). From a systematic-random series of coronal MRI images, total volumes of the hippocampal formation (V_{HF}) and whole brain (V_{brain}) were quantified by the Cavalieri-point counting method. The same sampling and estimation methods were used to quantify the same brain regions after perfusion and tissue processing. Strong correlations were found between V_{HF} and V_{brain} estimates from MRI images and histological sections. Agonal and tissue processing changes accounted for about 65 to 75% differences in cortical volumes between *in situ* and coverslipped sections. No differences were present in mean V_{HF} or mean V_{brain} for dtgAPP/PS1 compared to WT mice. These stereological studies of MRI neuroimages and postmortem tissue do not show cortical atrophy in association with widespread cortical deposition of AD-type amyloid plaques in aged dtg APP/PS1 mice, in contrast to the severe cortical atrophy in AD. Future studies with dtgAPP/PS1 mice will explore the possibility that high contrast ligands bound to mutant $A\beta$ proteins associated with amyloid plaques could facilitate early diagnosis of AD by ante-mortem neuroimaging.

Introduction

Reliable methods for the early diagnosis of Alzheimer's disease (AD), the most common form of dementia in persons over 65 years of age, would provide a major benefit to the therapeutic management of patients. Alois Alzheimer originally reported two primary neuropathological changes, neurofibrillary tangles and neuritic plaques, in a 51-y.o. woman with progressive dementia of unknown cause (Alzheimer 1907). Subsequent studies have indicated that plaques, rather than tangles, show the strongest association with the earliest symptoms of AD (Mirra et al., 1991, Matsuoka et al., 2001, McKeel et al., 2004, Tiraboschi et al., 2004). The other neuropathological changes that strongly correlates to the severity of dementia in AD is severe cortical brain atrophy (de la Monte 1989, Convit et al., 1993, Jobst et al., 1994, Stout et al., 1996, Mouton et al., 1998) and synaptic degeneration (DeKoskey and Scheff, 1990, Terry et al., 1991, Sze et al., 1997,). Therefore, based on the neuropathological evidence the presence of amyloid plaques and severe cortical atrophy appear to provide the most reliable markers to date for the early diagnosis and progression of AD.

These studies of AD neuropathology at autopsy are supported by recent MRI studies that show volume loss in the cortical regions of persons showing mild cognitive impairment (de Leon MJ et al., 2004). Because of the strong correlation between cortical atrophy and the severity of dementia in autopsy-confirmed AD cases (Mouton et al., 1998), volumetric studies of cortical tissue using ante-mortem magnetic resonance imaging (MRI) could be used to support the presumptive diagnosis of early AD (de Leon MJ et al., 2004). Thus, the presence of A β plaques and the progressive loss of cortical volumes could provide ante-mortem evidence for the diagnosis and progression of AD, respectively.

As a first step toward improving the ante-mortem diagnosis of AD, we addressed this issue using transgenic mice that co-express two mutant proteins from patients with inherited (familial) AD. The double transgenic expression of these mutant proteins, amyloid precursor protein (APP) and presenilin 1 (PS1), in mouse cortical tissue leads to the deposition of mutant β -amyloid (A β) and the formation of amyloid plaques that appear indistinguishable from those in AD. To quantify volumetric changes in the brains of dtg APP/PS1 mice and wild-type controls (WT), we applied the Cavalieri-point counting method that has been previously applied to the stereological estimation of cortical brain volume in humans on MRI images (Roberts et al, 2000, Howard et al., 2003) and autopsied tissue (Mouton et al., 1998, other refs), and histological sections from mice (Long et al., 1998, Mouton et al., 2002, Lei et al., 2003).

Methods and Materials

Mice for these studies were male and female dtg APP/PS1 and age- and gender-matched WT controls. Mice dtg and non-tg groups weighed between 25 and 28 g and were randomized at the start of the study into groups for MRI (n=13) or histology (n = 10). The age of mice in this study spanned the adult lifespan of the mice (4-28 mos).

MRI. Mice were anesthetized during MRI with 1.5~2.0 vol % isoflurane mixed with oxygen in a flow rate of 200 cm³/min. Oxygen and isoflurane were administered through a nasal cone mask. The mouse was placed in supine position at the center of a Varian 4.7 T NMR machine with 33 cm horizontal magnet bore. A 25 mm long, 20 mm i.d. (inner diameter) birdcage RF (radio frequency) coil was used. The coil was placed around the head of mouse. The coil was used as a RF transmitter and receiver. A balloon filled with D₂O was placed under the abdomen of the mouse and used as a respiratory sensor.

High resolution spin echo MRI. A MRI spin echo imaging sequence was used. The repetition time (TR) was 2.5 seconds and the echo time (TE) was 40 msec. The field-of-view was 14 mm x 14 mm and the matrix size was 256x256. The spatial resolution of the images was 55 μ m. The slice thickness was 1 mm. There were two sets of 15 images taken interleavedly. The total brain volume and hippocampal formation were measured by two investigators hand-drawing the outlines of the regions of interest and analyzed with Image Browser software (Varian Inc, Palo Alto, CA) (Figure X).

Histology. The mice were deeply anesthetized via CO₂ inhalation, then transcardially perfused with phosphate-buffered saline (PBS), 4% paraformaldehyde in 0.1 M PBS (pH 7.4) and postfixed in the 4% paraformaldehyde fixative overnight. The brains were transferred to a 30% sucrose phosphate buffer solution until they sank, then frozen in CO₂/isopentane and stored at -80°C until sectioning. For estimation of V_{HF} sampling was carried out the all sections through the hippocampal formation. Each brain was serially sectioned in the coronal plane on a sliding freezing microtome. Sections cut at an instrument setting of 50 μ m. were sampled in a systematic-random manner, i.e., random start in the first five sections then systematic for every 5th section. A similar approach was applied to sampling every 10th section of the total sections through a complete hemisphere for estimation of total brain volume (V_{brain}). Sampled sections were stained using routine cresyl violet for Nissl substance and coverslipped for microscopic examination (Figure X).

Stereology: Using computer assisted stereology system, volumes for MRI slices and tissue sections were estimated using the Cavalieri principle with point counting (Cavalieri 1635, Mouton 2002), as we have detailed previously for brain and hippocampal volumes in human, non-human primate, and rodent brains (Subbiah et al., 1996, Mouton et al., 1997, Mouton et al., 1998, Long et al., 1998).

$$V_{\text{ref}} = \sum \text{Area}_{\text{slices}} \cdot \text{Mean } t$$

where,

V_{ref} = Reference volume (hippocampal formation or whole brain, in mm³)

$\sum \text{Area}_{\text{slices}}$ = area on slice or section, in mm²

Mean t = mean post-processing section or slice thickness, in mm

In order to capture the majority of variability within- and between-mice for each group, data were collected until the coefficient of error (CE) was less than one-half of the biological

variability (Gundersen and Osterby 1981, Gundersen et al., 1999.). The results were calculated as mean (SEM) for each group and for each modality (MRI or histology).

Results

Using the Cavalieri-point counting method, volumes of hippocampal formation (V_{HF}) and whole brain (V_{brain}) were carried out on MRI and histology sections from dtg APP/PS1 and WT controls. Because there were insufficient numbers of mice of different ages for a proper study of age or gender effects, the results were collapsed across age and gender and analyzed for possible transgene effects [dtg APP/PS1 vs. non-Tg littermates (WT) controls] on volumes of hippocampal formation (V_{HF}) and whole brain (V_{brain}).

Table 1 shows comparison of mean volume estimates for hippocampal formation (V_{HF}) and whole brain (V_{brain}) related to the over-expression of human APP/PS1 mutations in the dtg mice. Volumetric analyses of the same regions on MRI images revealed mean (SEM) values for the dtg APP/PS1 mice [$V_{HF} = 30.4 (0.12) \text{ mm}^3$, $V_{brain} = 451.5 (4.31) \text{ mm}^3$], which were comparable to those for the WT controls [$V_{HF} = 30.7 (0.66) \text{ mm}^3$, $V_{brain} = 449.6 (0.54) \text{ mm}^3$].

Stereologic analyses of V_{HF} and V_{brain} on histological sections measured after all tissue processing showed no differences related to transgene expression. Figure X shows the mean (SEM) values for the dtg APP/PS1 mice [$V_{HF} = 4.6 (0.12) \text{ mm}^3$, $V_{brain} = 61.5 (1.12) \text{ mm}^3$], which were not different from the values for the WT controls [$V_{HF} = 4.8 (0.13) \text{ mm}^3$, $V_{brain} = 60.2 (2.05) \text{ mm}^3$].

Comparing the percentages of whole brain occupied by hippocampus [(mean V_{HF} / mean V_{brain}) • 100] for the two groups of dtg and non-tg mice did not reveal appreciable differences for volume estimates on MRI images [dtg APP/PS1 = 6.73% vs. WT = 6.83%] or histological sections [dtg APP/PS1 = 7.48% vs. WT = 7.97%].

Table 1. Summary of Cavalieri-point counting estimates of brain volumes [mean (SEM)] for analyses of MR images and histology sections. V_{brain} = total brain vlume, V_{HF} = total hippocampal formation volume, WT = wild-type.

Genotype	MRI(mm ³)	Histology(mm ³)	% shrinkage
WT			
V_{brain}	451.5 (4.31)	60.2 (2.05)	70
V_{HF}	30.4 (0.12)	4.8 (0.13)	69
$V_{brain}/ V_{HF}(\%)$	6.73±1.34	7.97	
Dtg APP/PS1			
V_{brain}	449.6 (0.54)	61.5 (1.12)	73
V_{HF}	30.7 (0.66)	4.66 (0.12)	72
$V_{brain}/ V_{HF}(\%)$	6.88±2.36	7.48	

Kin: check the above data with Jahn. When I calculate shrinkage (% shrinkage = [(MRI volume – Histology volume)/MRI volume] • 100] the results are in the range of 80 to 90%. For example,

	MRI	Histology	% shrinkage
V _{brain}	451.5	60.2	$[(451.5-60.2)/451.5] \cdot 100 = 86.67\%$

Discussion

Stereological methods were used to estimate total volume of whole brain and hippocampal formation on MR images and histological sections in dtg APP/PS1 mice and WT controls. Spin-echo T1-weighted MR was used to capture images through the entire brain and hippocampus at scan times of 1.5 hours at 4.7 T NMR machine. Cavalieri-point counting stereology was used to quantify V_{brain} and V_{HF} to 8-12 systematic-random series of coronal MRI images through each reference space. The same method was used to quantify the same brain regions on age-matched dtg APP/PS1 and WT mice after perfusion and tissue processing for microscopic examination.

The consistency of volume estimates in the same brain regions of dtg APP/PS1 and WT mice confirmed the robustness of the Cavalieri-point counting approach for both ante-mortem images and postmortem tissue. Also, the interpersonal variation of the volumetric measurement on the MRI images is minimum, less than 2%. Since the aim of this study was to quantify volumes, it was not necessary to co-register matched areas on the same coronal level between the MRI images and histological tissues. For both dtg APP/PS1 and WT mice there are significant agonal and fixation effects on brain volumes, about 75% volume loss between MRI images and the completion of all tissue processing. This total tissue shrinkage can be further partitioned into two parts: ~ 15% shrinkage from agonal and fixation-induced changes between volume measurements during MRI and perfusion fixation, and, ~ 50-60% shrinkage during the process of processing fixed brain into sections for microscopic visualization (e.g., freezing microtomy, drying, staining with cresyl violet, coverslipping). Finally, the correlation between volume measurements on the same regions on MRI images and histological sections indicates that the methods for immobilization and monitoring of cardiac and respiratory function did not cause significant blurring of the MRI images.

The mice in this study overexpress high levels of mutant A β in parenchyma, which leads to the formation of amyloid plaques histologically similar to those in AD. The mice in the present study show hyper-accumulation of the 42 amino acid A β residue (Jankowsky et al., 2004) and A β containing amyloid plaque formation beginning around age 4-5 months of age. In a related line of dtg APP/PS1 mice, the time course for the deposition of A β -containing amyloid plaque load (amyloid load) increases rapidly in cortex and hippocampus during the age range of the mice in the present study (Gordon et al., 2001). At 7 months of age, we have previously reported evidence for vascular abnormalities (reduced capillary branching) in these dtg APP/PS1 mice (Lee et al., *in press*). Two previous studies, one using this line of dtg APP/PS1 mice (Savonenko

et al., *in press*) and another using mice with the single Swedish mutation (Tg₂₅₇₆, Dedeoglu et al., 2004), report altered neurochemical profiles in mice greater than 18 months of age.

Our findings in dtg APP/PS1 mice aged 18-20 mos of age indicate that widespread deposition of AD-type amyloid plaques in brains of APP1/PS1 mice is not closely associated with ante-mortem slightly T2-weighted MRI or postmortem evidence of whole brain and hippocampal atrophy. Among the range of possible explanations for this discrepancy could be the difference in methods of tissue processing (e.g., perfusion versus immersion fixation). The strong correlation between volume estimates from MRI and processed sections, however, would appear to eliminate this factor as a confounding variable. These findings suggest that the mechanisms that lead to the formation of amyloid plaques in cortical brain regions of dtg APP/PS1 mice appears to differ in meaningful, yet undefined ways from the neurobiological processes that cause plaque formation in AD.

The ultimate goal of this line of research is the ante-mortem visualization of amyloid plaques in cortical brain regions of persons with preclinical AD (Benveniste et al., 1999, Sohhi-Jadid et al., 1999, Poduslo et al., 2002, DeLeon et al., 2004). The present findings encourage our efforts to find correlations between ante-mortem neuroimaging and underlying histopathology in the brains of dtg APP/PS1 mice. A recent MRI study of dtg APP/PS1 mice reported differences to non-tg controls in the transverse relaxation time T_2 , in several regions of cortical grey matter (hippocampus, cingulate, and retrosplenial cortex), which may reflect impaired cell physiology in these regions (Helpert et al. 2004). The absence of differences in T1-weighted or proton density weighted MRI images suggests that heavily T2-weighted images may be more sensitive to amyloid accumulation in the dtg APP/PS1 mice. Previous studies using $T_{1\rho}$ ("T-1-rho")-weighted MRI has been moderately successful in demonstrating amyloid plaques *in vivo* based on local variations in protein content (Borthakur et al., 2003). Enhanced visualization of amyloid plaques in dtg APP/PS1 mice has been demonstrated by pre-injecting A β peptides magnetically labeled with gadolinium or iron oxide nanocrystals (Wadgheri et al., 2003). Our studies will continue to develop the optimal MRI parameters to visualize ligands that effectively cross the blood brain barrier and bind to microscopic targets associated with AD neuropathology.

Acknowledgements. The authors would like to recognize the Public Health Service for funding support for these studies (NIH grant 1R43EB001605-01, RCMI/NCRR/NIH G12RR03048, and DAMD17-00-1-0291).

References

1. Alzheimer, A. Ueber eine eigenartige Erkrankung der Hirnrinde. Allgemeine Zeitschrift für Psychiatrie 64:146-148, 1907.
2. Borthakur A, Urya K, Chively SB, Poptani H, Corbo M, Charagundla SR, Trojanoqski JQ, Lee VM, Reddy R, In Vivo $T_{1\rho}$ Weighted MRI Of Amyloid Transgenic Mouse Model Of Alzheimer's Disease. Proc. Intl. Soc. Mag. Reson. Med. 11:2039, 2003.
3. Borchelt, DR., Ratovitski, T., van Lare, J., Lee, MK., Gonzales, V., Jenkins, NA., Copeland, NG., Price, DL., and Sisodia, SS., Accelerated amyloid deposition in the brains

of transgenic mice coexpressing mutant presenilin 1 and amyloid precursor proteins., *Neuron*, 19 (1997) 939-45.

4. Cavalieri, B. *Geometria indivisibilibus continuorum*. Bononi: Typis Clementis Ferronij, 1635. Reprint from: *Geometria degli indivisibili*. Torino: Unione Tipografico-Editrice Torinese, 1966.
5. Convit, A., de Leon, M. J., Golomb, J., George, A. E., Tarshish, C. Y., Bobinski, M., Tsui, W., De Santi, S., Wegiel, J., Wisniewski, H. Hippocampal atrophy in early Alzheimer's disease: anatomic specificity and validation. *Psychiatr. Q.* 64:371-387, 1993.
6. DeKosky, S. T., Scheff, S. W. Synapse loss in frontal cortex biopsies in Alzheimer's disease: correlation with cognitive severity. *Ann. Neurol.* 27:457-464, 1990.
7. de la Monte, S. M. Quantitation of cerebral atrophy in preclinical and end-stage Alzheimer's disease. *Ann. Neurol.* 25:450-459, 1989.
8. de Leon MJ, DeSanti S, Zinkowski R, Mehta PD, Pratico D, Segal S, Clark C, Kerkman D, DeBernardis J, Li J, Lair L, Reisberg B, Tsui W, Rusinek H. MRI and CSF studies in the early diagnosis of Alzheimer's disease. *J Intern Med.* 256:205-23, 2004.
9. Gordon MN, Holcomb LA, Jantzen PT, DiCarlo G, Wilcock D, Boyett KW, Connor K, Melachrinou J, O'Callaghan JP, Morgan D. Time Course of the Development of Alzheimer-like Pathology in the Doubly Transgenic PS1APP Mouse. *Exp Neurol* 173, 183-195 (2002).
10. Gundersen HJG, Østerby, R (1981) Optimizing sampling efficiency of stereological studies in biology: Or "Do more less well." *J Microsc* 121:65-73.
11. Gundersen HJG, Jensen EV, Kieu K, Nielsen J (1999) The efficiency of systematic sampling in stereology - revisited. *J Microsc* 193:199-211.
12. Helpert, J.A., Lee, S-P., Falangol, M.F., Dyakin, V.V., Bogart, A., Ardekani B., Duff, K., Branc, C., Wisniewski, T., de Leon, M.J., Wolf, O., O'Shea, J., Nixon, R.A.. MRI assessment of neuropathology in a transgenic mouse model of Alzheimer's disease. *Magn Reson Med* 51:794-798, 2004.
13. Jankowsky, J., Fadale, D.J., Andersen, J.K., Xu, G., Gonzales, V., Jenkins, N.A., Copeland, N.G., Lee, M.K., Younkin, L.H., Wagner, S.L.,
14. Younkin, S.G., Borchelt, D.R., 2004. Mutant Presenilins Specifically Elevate The Levels Of The 42 Residue H-Amyloid Peptide In Vivo: Evidence For Augmentation Of A 42-Specific Gamma Secretase. *Hum. Mol. Genet.* 13, 159- 170.
15. Jobst, K. A., Smith, A. D., Szatmari, M., Esiri, M. M., Jaskowski, A., Hindley, N., McDonald, B., Molyneux, A. J. Rapidly progressing atrophy of medial temporal lobe in Alzheimer's disease. *Lancet* 343:829-830, 1994.
16. Jack CR, Garwood M, Wengenack TM, Borowski B, Curran GL, Lin J, Adrian G, Grohn OHJ, Grimm R, Podulso JF, In Vivo Visualization of Alzheimer's Amyloid Plaques by Magnetic Resonance Imaging in Transgenic Mice without a Contrast Agent. *Magn Reson Med* 52:1263-1271 (2004).
17. Lee GD, Aruna JH, Barrett JM, Lei D-L, Ingram DK, Mouton PR. Stereological Analysis Of Microvascular Parameters In A Double Transgenic Model Of Alzheimer's Disease. *Brain Res Bull*, *in press*.
18. Lei DL, Long JM, Hengemihle J, O'Neill J, Manaye KF, Ingram DK, Mouton PR. Effects of estrogen and raloxifene on neuroglia number and morphology in the hippocampus of aged female mice. *Neuroscience.* 121:659-66 (2003).

19. Long JM, Kalehua AN, Muth NJ, Calhoun ME, Jucker M, Hengemihle JM, Ingram DK, Mouton PR. Stereological analysis of astrocyte and microglia in aging mouse hippocampus. *Neurobiol Aging*. 19:497-503, 1998.
20. Mirra, S. S., Hart, M. H., Terry, R. D. Making the diagnosis of Alzheimer's disease. A primer for practicing pathologists. *Arch. Pathol. Lab. Med.* 117:132-144, 1993.
21. Mouton PR, Price DL, Walker LC. Empirical assessment of synapse numbers in primate neocortex. *J Neurosci Methods* 75:119-26 (1997). Mouton PR, Martin LJ, Calhoun ME, Dal Forno G, Price DL.
22. Cognitive decline strongly correlates with cortical atrophy in Alzheimer's dementia. *Neurobiol Aging*. 19:371-7 (1998).
23. Mouton, PR Principles and Practices of Unbiased Stereology: An Introduction For Bioscientists, Johns Hopkins University Press, Baltimore (2002).
24. McKeel DW, Price JL, Miller JP, Grant EA, Xiong C, Berg L, Morris JC. Neuropathologic criteria for diagnosing Alzheimer disease in persons with pure dementia of Alzheimer type. *J Neuropathol Exp Neurol*. 2004 Oct, 63(10):1028-37.
25. Savenenko A, Xu GM, Melnikova T, Morton J, Gonzales V, Wong M, Price DL, Tang F, Markowska AL, Borchelt DR. Episodic-like memory deficits in the APPswe/PS1dE9 mouse model of Alzheimer's disease: relationship to β -amyloid deposition and neurotransmitter abnormalities. *Neurobiol Disease*, *in press*.
26. Stout, J. C., Jernigan, T. L., Archibald, S. L., Salmon, D. P. Association of dementia severity with cortical gray matter and abnormal white matter volumes in dementia of the Alzheimer type. *Arch. Neurol*. 53:742-749, 1996.
27. Terry, R. D., Masliah, E., Salmon, D. P., Butters, N., DeTeresa, R., Hill, R., Hansen, L. A., Katzman, R. Physical basis of cognitive alterations in Alzheimer's disease: synapse loss is the major correlate of cognitive impairment. *Ann. Neurol*. 30:572-580, 1991.

MR Image Enhancement by Tumor Cell Targeted Immunoliposome Complex Delivered Contrast Agent

Paul C. Wang, PhD¹, Ercheng Li, PhD¹, Renshu Zhang, MD¹, Huaifu Song, BS¹, Kathleen Pirollo, PhD², Esther H. Chang, PhD².

¹Howard University, USA, ²Georgetown University, USA.

Paramagnetic contrast agents such as gadolinium chelates have been used to enhance MR image contrast by disturbing the local magnetic field and the magnetization of surrounding proton spins. The uptake of the contrast agent into the tumor interstitial space is based upon permeation of contrast agent through arterioles and its diffusion within intercellular space. The uptake process is not specific. We have made use of a cationic immunoliposome system that employs a single-chain antibody variable fragment (scFv) to target a liposome-contrast agent complex preferentially to the human transferrin receptor (TfR) of cancer cell. Cationic liposomes are composed of positively charged lipid bilayers that are complexed to gadolinium chelates, Magnevist, by simple mixing. The resulting complex has a net positive charge that facilitates transfection of the cells, and a small size that allows penetration through the capillaries to the tumor cells. Magnevist is diluted in water and added to scFv-Lip at a defined ratio. The equivalent dose of Magnevist is 0.3 mM/kg. Human leukemic cells K562 were transfected with the solution containing TfR-scFv-Lip-Magnevist complex, or Magnevist only. After transfection, the cells were cultured for additional 48 hours. The cells then were pelleted for MRI study. T1-weighted MR images (SE TR/TE, 1000ms/13ms) of cell pellets show an intensity increase of 6 folds for TfR-scFv-Lip-Magnevist complex compared to Magnevist only. Also, a study of transfection time shows the intensity change reaches a plateau after 60 minutes exposure. The advantages of targeted liposome as contrast agent delivery vehicle are its low toxicity, simplicity of preparation, its relative stability, and most significantly its ability to preferentially target tumor cells and efficiently transfer the contrast agent to them. Therefore use of this delivery system has the potential to enhance the sensitivity of the contrast agent.

(Presented at the Third Annual Meeting of the Society of Molecular Imaging at St. Louis, MO, September 9-12, 2004)

34th Annual Meeting of the Society of Neuroscience. October 23-27, 2004, San Diego, CA

In-Vivo and In-vitro Stereological Analysis of Hippocampal and Brain Volumes in Young and Old APP/PS1 Mice Using Magnetic Resonance Neuroimages

Manaye, K.F.^{1*}, Wang, P.¹, O'Neil J.¹, Armand Oei¹, Huaifu Song¹, Tizabi Y.¹, Ingram, D.K.², Mouton, P.R.^{2,3}

¹Howard University School of Medicine;

²Laboratory of Experimental Gerontology, National Institute on Aging, NIH, Baltimore, MD;

³Stereology Resource Center, Chester, MD.

Previous stereological studies of cortical volumes in human brains at autopsy show only slight changes during normal aging. In contrast, autopsied brains from patients suffering neurological disease, including acquired immunodeficiency syndrome (AIDS) and Alzheimer's disease (AD), show significant loss (atrophy) of cortical and whole brain volumes compared to age-matched controls. In the case of AD the severity of cortical atrophy is highly correlated to the severity of cognitive impairment (Mouton et al., *Neurobiol Aging* 19:371-377, 1998). Early detection of cortical atrophy would help to better understand the natural history of neurodegenerative changes and improve the efficacy of strategies for therapeutic management of these diseases. We addressed this issue using high-resolution magnetic resonance imaging (MRI) to visualize the right hippocampal formation and right hemisphere of mice double transgenic for two mutant proteins associated with AD (amyloid precursor protein and presenilin-1). Young and aged dtg APP/PS1 mice were imaged using a spin-echo T1-weighted MRI imaging technique.

Total volumes of right hemisphere (Vbrain), and total right hippocampal formation (VHF) were estimated from systematic-random series of coronal MRI images using point counting-Cavalieri method. We estimated the hemispheric and hippocampal formation volumes in the brains perfused and processed for histology, and the estimates of Vbrain, and VHF were repeated after final tissue processing. The preliminary findings In-vivo for WT and dtg APP/PS1 mice show a 15 % reduction in volume of hippocampal formation and no change in the volume of the brain. The In-vitro analysis showed consistent shrinkage of 65-75% for each examined brains.

These stereological studies of mouse MRI images document the changes in brain volumes associated with agonal and tissue processing, and support quantitative neuroimaging for characterization of rodent models of neurological disease. Additional studies will address whether the age-related changes in cortical brain volumes in dtg APP/PS1 mice mimic the patterns that occur in AD.

Supported by intramural and extramural funding from the U.S. Public Health Service. DAMD-17-00-1-0291 and RCMI/NCRR/NIH 2G12RR003048

Increased Transport of Trifluoperazine Across the Blood-Brain-Barrier Due to Modulation of P-glycoprotein

¹Paul C Wang, ²Adorjan Aszalos, ¹Ercheng Li, ¹Renshu Zhang, ¹Huafu Song, ¹Raymond Malveaux

¹Department of Radiology, Howard University, Washington, DC

²National Cancer Institute, Bethesda, MD

Elderly patients and patients with cancer are often treated with a combination of therapies for secondary illnesses such as depression, and cardiopulmonary diseases in addition to their primary illnesses. The potential for drug-drug interaction under these conditions is high. Such interactions may cause changes in the pharmacokinetics, especially for drugs with narrow therapeutic indices. These changes can alter efficacy and toxicity of the administered drugs. Drug-drug interactions may occur due to interaction of common metabolic pathways, but can also be caused by interference at the P-glycoprotein (Pgp) level. Pgp, which is a nonspecific transport protein, is expressed constitutively at the blood-brain-barrier (BBB), intestine, kidney, and liver. Interaction at the blood-brain barrier may occur if Pgp is blocked by a drug, allowing a concomitantly administered second drug, which would not penetrate brain if administered singly, to be able to penetrate the brain freely. The potential for drug-drug interactions is not routinely studied at the Pgp level during drug development. Its presence is assumed only after unexpected clinical symptoms arise. In this study, we used a dynamic NMR method based on detection of a fluorinated drug, trifluoperazine (TFP), in combination with an immune suppressor, cyclosporin A (CsA), to monitor the drug penetration through the blood-brain-barrier due to Pgp modulation.

Sprague-Dawley rats, weight 100-400 g, were used. The rats were first anesthetized by i.p. injection of sodium pentobarbital (40 mg/kg). A catheter (0.26 mm i.d.) was then inserted into the tail vein for later drug infusions. A Pgp modulator, cyclosporin A (15 mg/kg) was administered 15 min before trifluoperazine (25 mg/kg) was injected. ¹⁹F NMR using a Varian 4.7 T machine was utilized to detect trifluoperazine in the brain. A 22 x 17 mm RF coil was positioned immediately adjacent to the rat skull. A small bulb containing trifluoroacetic acid was used as an extern reference. After shimming and tuning, a series of 10 minutes spectra were obtained. The repetition time was one second. The same animal was used as control without cyclosporin A. The test results of five different rats were averaged for each data point.

In Figure 1, the spectrum A shows a control, in which only TFP was administered. The spectrum B shows a 22% increase of TFP crossing BBB in a 200 gm rat after co-administering a Pgp modulator, cyclosporin A. Figure 2 shows the increased amount of TFP crossing BBB as function of age (or body weight). Younger rats weighing below 150 gm showed no increase of TFP penetration. However, for older adult rats weighing more than 200 gm, a 20-25% increase of TFP crossing BBB was evident.

This experiment has demonstrated that a concomitantly administered Pgp modulator enhanced the amount of TFP, an antipsychotic drug, to cross blood-brain-barrier in vivo. The pharmacology of this noninvasive model for increasing the crossing of drugs over the BBB due to drug-drug interactions was based on previously attained knowledge about how to modulate Pgp, and also because the drug was able to be detected by in vivo ¹⁹F NMR spectroscopy. It also demonstrated that Pgp modulation is more problematic for older rats. In the case of polypharmacy, particularly for elderly or cancer patients, drug-drug interaction is not always understood. The noninvasive dynamic NMR technique can be a very useful tool to study multidrug interactions in drug development.

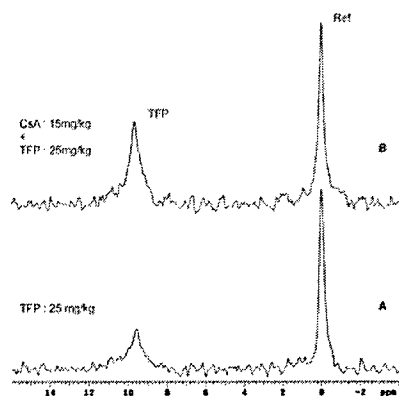


Fig 1

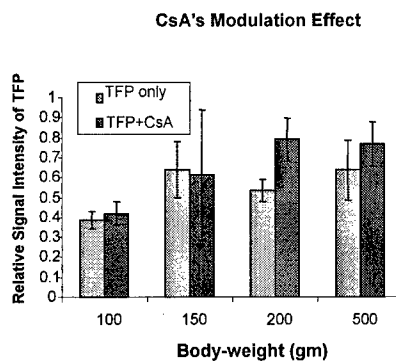


Fig 2

(This work was supported by grants: DAMD-17-00-1-0291 and RCMI/NCRR/NIH 2G12RR003048).

NMR Studies of Phosphorus Metabolites of Breast Cancer Cells Using An Improved Cell Perfusion System

Applications for the Improved NMR Perfusion System for Breast Cancer Cell Study

Chikezirim L. Agwu*, Jianwei Zhou[#], Ercheng Li[#], Raj Sridhar and Paul Wang[#]

*Department of Biochemistry and Molecular Biology, Howard University Hospital

[#]Department of Radiology, Howard University Hospital, Washington, DC 20060, USA

ABSTRACT

Nuclear Magnetic Resonance imaging (MRI) and magnetic resonance spectroscopy (MRS) have been increasingly used in cancer research over the recent years due to the noninvasiveness of these techniques and the ability of measuring specific intracellular metabolites in vivo. P^{31} NMR has been used to study the high energy phosphorus metabolites in tumors such as It has also been used to monitor the effectiveness of cancer treatment. Since the NMR signals of the metabolites in cells are weak and the NMR study usually are long. During the long data acquisition time, the cancer cells need to be maintained in a good living environment. In this paper, we present an improved NMR cell-perfusion system, which was used to study the phosphorus metabolites of breast cancer cells for an extended period. The improved perfusion system is driven by a peristaltic pump. The portion of the system before the pump is under negative pressure, and the portion after the pump is under positive pressure. This design helps the removal of air bubbles trapped in the perfusion medium and avoid the degradation of the quality of NMR spectrum. Using this perfusion system, NMR study of the breast cancer cells can be extended for more than a week not hours as it used to be. The ^{31}P NMR spectrum of the MCF7/WT breast cancer cells shows three distinct phases, which reflect the proliferation of the cells. Study of oxygenation of the agarose-encased cells in this perfusion system suggests that the cells utilized aerobic respiration. The ability for this perfusion system to maintain cells viable for more than a week allowed us to determine the longitudinal relaxation times (T1 values) of the ^{31}P metabolites of MCF7/WT cells in vitro. A progressive saturation recovery NMR technique was used for T1 measurement. Accurate T1 values are crucial in designing P^{31} MRS studies. This study has demonstrated that the long time bubble-free NMR cell perfusion system could be a useful tool for in vitro breast cancer research.

9th RCMI International Symposium on Health Disparities, Baltimore, MD, Dec 8-11, 2004

In-Vivo and In-vitro Stereological Analysis of Hippocampal and Brain Volumes in Young and Old APP/PS1 Mice Using Magnetic Resonance Neuroimages

Manaye, K.F.^{1*}, Wang, P.¹, O'Neil J.¹, Armand Oei¹, Huaifu Song¹, Tizabi Y.¹, Ingram, D.K.², Mouton, P.R.^{2,3}

1Howard University School of Medicine;

2Laboratory of Experimental Gerontology, National Institute on Aging, NIH, Baltimore, MD;

3Stereology Resource Center, Chester, MD.

Previous stereological studies of cortical volumes in human brains at autopsy show only slight changes during normal aging. In contrast, autopsied brains from patients suffering neurological disease, including acquired immunodeficiency syndrome (AIDS) and Alzheimer's disease (AD), show significant loss (atrophy) of cortical and whole brain volumes compared to age-matched controls. In the case of AD the severity of cortical atrophy is highly correlated to the severity of cognitive impairment (Mouton et al., *Neurobiol Aging* 19:371-377, 1998). Early detection of cortical atrophy would help to better understand the natural history of neurodegenerative changes and improve the efficacy of strategies for therapeutic management of these diseases. We addressed this issue using high-resolution magnetic resonance imaging (MRI) to visualize the right hippocampal formation and right hemisphere of mice double transgenic for two mutant proteins associated with AD (amyloid precursor protein and presenilin-1). Young and aged dtg APP/PS1 mice were imaged using a spin-echo T1-weighted MRI imaging technique.

Total volumes of right hemisphere (V_{brain}), and total right hippocampal formation (V_{HF}) were estimated from systematic-random series of coronal MRI images using point counting-Cavalieri method. We estimated the hemispheric and hippocampal formation volumes in the brains perfused and processed for histology, and the estimates of V_{brain} and V_{HF} were repeated after final tissue processing. The preliminary findings In-vivo for WT and dtg APP/PS1 mice show a 15 % reduction in volume of hippocampal formation and no change in the volume of the brain. The In-vitro analysis showed consistent shrinkage of 65-75% for each examined brains.

These stereological studies of mouse MRI images document the changes in brain volumes associated with agonal and tissue processing, and support quantitative neuroimaging for characterization of rodent models of neurological disease. Additional studies will address whether the age-related changes in cortical brain volumes in dtg APP/PS1 mice mimic the patterns that occur in AD.

(Supported by intramural and extramural funding from the U.S. Public Health Service. DAMD-17-00-1-0291 and RCMI/NCRR/NIH 2G12RR003048)

9th RCMI International Symposium on Health Disparities, Baltimore, MD, Dec 8-11, 2004